Toni Pasanen

Surface passivation of black silicon phosphorus emitters

School of Electrical Engineering

Thesis submitted for examination for the degree of Master of Science in Technology.

Espoo 13.1.2017

Thesis supervisor:

Prof. Hele Savin

Thesis advisor:

D.Sc. (Tech.) Ville Vähänissi

Aalto University
School of Electrical Engineering

AALTO UNIVERSITY
SCHOOL OF ELECTRICAL ENGINEERING

ABSTRACT OF THE
MASTER'S THESIS

Author: Toni Pasanen

Title: Surface passivation of black silicon phosphorus emitters

Date: 13.1.2017 Language: English Number of pages: 10+59

Department of Electronics and Nanoengineering

Professorship: Micro and Nanoelectronics

Supervisor: Prof. Hele Savin

Advisor: D.Sc. (Tech.) Ville Vähänissi

Black silicon (b-Si) has been of interest of the photovoltaic community already some time due to its excellent light absorption properties. The difficulties in the surface passivation of b-Si have recently been overcome with atomic layer deposited (ALD) Al_2O_3. However, there is no solution yet presented for the dominating p-type solar cells with an n+ emitter, i.e. a heavily doped layer near the cell surface, as Al_2O_3 provides only limited passivation for such emitters due to its negative fixed charge. This problem is enhanced in b-Si since its passivation relies more heavily on the field-effect passivation.

In this thesis, the addressed problem is approached by searching thin film materials with positive fixed charge. Based on a literature review, the most promising passivation scheme, SiO_2/Al_2O_3 dielectric stack, is selected and studied experimentally on phosphorus doped b-Si surfaces. First, electrical properties between thermally oxidized and ALD SiO_2 interlayer are compared using minority carrier lifetime and contactless C–V measurements. The measurements reveal that the charge in the stacks with thermal SiO_2 possesses unsuitable polarity while the charge in the ALD stacks is found to be positive. Furthermore, the interface defect density between silicon and the ALD stack is found to be 10^{11} cm^{-2}eV^{-1}, which should be sufficiently low for efficient emitter surface passivation.

The ALD SiO_2/Al_2O_3 stacks with positive fixed charge are then applied to b-Si phosphorus emitters. The stacks are found to passivate planar emitters efficiently and they work surprisingly well also on b-Si which has not been reported earlier. The level achieved on planar surfaces cannot fully be reached but it was expected due to a larger surface area. Since the optimization of the emitter itself was left out of the scope of this study, excessive doping limits the measured emitter saturation current. Nevertheless, the results suggest that the actual surface passivation works which was the goal of this study. The results thus provide a significant step towards the implementation of b-Si for commercial p-type silicon solar cells.

Keywords: black silicon, surface passivation, phosphorus emitter, atomic layer deposition (ALD), SiO_2, Al_2O_3

AALTO-YLIOPISTO
SÄHKÖTEKNIIKAN KORKEAKOULU

DIPLOMITYÖN
TIIVISTELMÄ

Tekijä: Toni Pasanen

Työn nimi: Musta pii -fosforiemitterien pintapassivointi

Päivämäärä: 13.1.2017 Kieli: Englanti Sivumäärä: 10+59

Elektroniikan ja nanotekniikan laitos

Professuuri: Mikro- ja nanoelektroniikka

Valvoja: Prof. Hele Savin

Ohjaaja: TkT Ville Vähänissi

Musta pii on jo jonkin aikaa herättänyt mielenkiintoa aurinkokennoyhteisössä erinomaisten absorptio-ominaisuuksiensa ansiosta. Ongelmat mustan piin pintapassivoinnissa on hiljattain onnistuttu ratkaisemaan atomikerroskasvatetulla (ALD) alumiinioksidilla (Al_2O_3). Toimivaa ratkaisua ei ole kuitenkaan vielä toistaiseksi esitetty markkinoita hallitseville p-tyypin aurinkokennoille. Näiden kennojen n+ emitteriä, eli kennon pinnan lähellä olevaa vahvasti seostettua kerrosta, ei pystytä passivoimaan kunnolla Al_2O_3:lla materiaalin sisältämien negatiivisten varausten vuoksi. Ongelma korostuu entisestään mustalla piillä, jonka passivointi tukeutuu vahvasti varausten luomaan sähkökenttään.

Tässä työssä ongelmaa lähestytään etsimällä ohutkalvoja, jotka sisältävät positiivisia kiinteitä varauksia. Kirjallisuuskatsauksen perusteella lupaavinta vaihtoehtoa, SiO_2/Al_2O_3-kaksoiseristekerrosta, tutkitaan kokeellisesti fosforilla seostetulla mustalla piillä. Ensin verrataan termisellä oksidoinnilla ja ALD:llä valmistettujen SiO_2-välikerrosten sähköisiä ominaisuuksia vähemmistövarauksenkuljettajien elinaika- ja kontaktittomilla kapasitanssi–jännitemittauksilla. Mittaukset paljastavat termisesti kasvatetun kalvon varauksen olevan polaarisuudeltaan väärä, kun taas ALD:llä kasvatetun kaksoiskerroksen varaukset ovat positiivisia. Lisäksi piin ja ALD-kaksoiskerroksen rajapinnan kidevirhetiheydeksi mitataan $10^{11}\,\mathrm{cm^{-2}eV^{-1}}$, jonka pitäisi olla riittävän matala tehokkaaseen emitterin pintapassivointiin.

ALD SiO_2/Al_2O_3-kaksoiskerroksia sovelletaan seuraavaksi musta pii -fosforiemittereihin. Kaksoiskerroksen havaitaan passivoivan planaarit emitterit tehokkaasti, ja ne toimivat myös mustalla piillä yllättävän hyvin, mitä ei ole raportoitu aikaisemmin. Mustalla piillä ei aivan saavuteta planaarien tasoa, mikä oli odotettavaa suuremman pinta-alan vuoksi. Koska työn tarkoituksena ei ollut itse emitterin optimointi, voimakas seostus rajoittaa mitattua emitterisaturaatiovirtaa. Tulokset kuitenkin viittaavat siihen, että itse pintapassivointi toimii, mikä oli työn tavoite. Tulokset ovat täten merkittävä askel kohti mustan piin soveltamista kaupallisissa p-tyypin piiaurinkokennoissa.

Avainsanat: musta pii, pintapassivointi, fosforiemitteri, atomikerroskasvatus, SiO_2, Al_2O_3

Preface

This thesis is an output of work performed in the Electron Physics Group at the Department of Micro and Nanosciences of Aalto University School of Electrical Engineering. The study is part of the BLACK project supported under the umbrella of SOLAR-ERA.NET by TEKES, the Finnish Funding Agency for Innovation. The experimental part of the work was performed in the cleanroom facilities of OtaNano - Micronova Nanofabrication Centre of Aalto University.

First of all, I want to thank Professor Hele Savin for giving me the opportunity to be a part of her research group for more than one and a half years. In addition, I am grateful for her efforts in guiding the research to the correct direction. I am also thankful to my advisor Ville Vähänissi. Without his guidance regarding the structure of this thesis, this work would not have been as coherent entirety as it is. Furthermore, his expertise in emitter design and characterization and cleanroom work in general was highly valuable, not forgetting another emitter expert Hannu Laine. Päivikki Repo's extensive experience in surface passivation of black silicon was of invaluable help and I am grateful to her for sharing that knowledge with me. I also want to thank another researcher working with black silicon surface passivation, Guillaume von Gastrow, for being the very first person who introduced me to black silicon and the processing of lifetime samples when I started in EPG.

One easily gets blind to his own text and therefore, opinions from external readers are of great benefit. Heli Seppänen and Niina Kajovuori are thanked for their relevant comments regarding the general formatting of the text and for spotting minor mistakes that had passed my own scan. In addition, a thank you goes to my colleague Juha Heinonen for being a daily lunch company and all my friends for giving me something else other than work to think about. Finally, I want to thank my family for the support throughout my studies and life in general.

Otaniemi, 11.1.2017

Toni Pasanen

Contents

Abstract ii

Abstract (in Finnish) iii

Preface iv

Contents v

Symbols and abbreviations vii

1 Introduction 1

2 Theory and background 3
2.1 Operating principle of a solar cell . . . 3
2.2 Minority carrier lifetime and recombination . . . 5
2.2.1 Bulk recombination . . . 5
2.2.2 Surface recombination . . . 7
2.3 Surface passivation . . . 9
2.3.1 Oxide charge . . . 10
2.4 Black silicon . . . 11
2.4.1 Optical properties . . . 11
2.4.2 Fabrication . . . 13
2.4.3 Electrical properties . . . 13
2.5 Solar cell emitter . . . 14
2.5.1 Emitter in black silicon . . . 15
2.6 Thin film materials for surface passivation of n+ emitters . . . 17
2.6.1 Aluminium oxide . . . 17
2.6.2 Thermal silicon dioxide . . . 18
2.6.3 Hydrogen-annealed SiO_2 . . . 19
2.6.4 Silicon nitride and amorphous silicon . . . 20
2.6.5 Stacked ALD SiO_2/Al_2O_3 . . . 21

3 Experimental methods **24**
3.1 Atomic layer deposition . . . 24
3.2 Quasi-steady-state and transient photoconductance decay methods . . . 26
3.3 Extraction of emitter saturation current density . . . 27
3.4 Corona oxide characterization of semiconductor . . . 28
3.5 Charge density from contact potential difference . . . 32
3.6 Characterization of emitter doping profiles . . . 33

4 Results and discussion **35**
4.1 Hydrogen annealed SiO_2 35
4.2 Thermal vs. ALD SiO_2 interlayer for stacked films 36
4.3 Film and passivation properties of ALD SiO_2/Al_2O_3 38
4.4 Emitter formation 43
4.5 Phosphorus emitter passivation 45

5 Conclusions **49**

References **51**

Symbols and abbreviations

Symbols

A	junction area
a	absorptance
B	radiative recombination coefficient
$C_{\mathrm{n/p}}$	Auger recombination coefficient for electrons/holes
D	diffusivity
$D_{\mathrm{e/h}}$	electron/hole diffusivity
D_{it}	interface defect density [$\mathrm{cm^{-2}eV^{-1}}$]
ΔE_{g}	band gap narrowing
E_{i}	intrinsic Fermi energy
E_{t}	trap state energy / surface state energy
FF	fill factor
$G(t)$	time-dependent generation rate
I	current
I_0	saturation current
I_{L}	light-generated current
I_{m}	current at maximum power point
I_{sc}	short-circuit current
$J_{0\mathrm{e}}$	emitter saturation current density
k	Boltzmann constant
L	diffusion length
n	electron density
n_0	equilibrium electron density
$N_{\mathrm{A/D}}$	acceptor/donor density
N_{dop}	net dopant concentration
n_{i}	intrinsic carrier concentration
$n_{\mathrm{i,eff}}$	effective intrinsic carrier concentration
N_{it}	interface defect density [$\mathrm{cm^{-2}}$]
n_{s}	electron surface concentration
Δn	excess carrier density
p	hole density
p_0	equilibrium hole density
P_{in}	incident power
p_{s}	hole surface concentration
q	elementary charge
Q_{c}	corona charge
Q_{f}	fixed oxide charge
Q_{it}	interface trapped charge
$Q_{\mathrm{it}}^{\mathrm{FB}}$	interface trapped charge under the flat band condition
Q_{m}	mobile oxide charge
Q_{ot}	oxide trapped charge
Q_{ox}	oxide charge

$Q_{\rm sc}$	charge in the space charge region
$Q_{\rm surf}$	initial charge on the dielectric surface
$Q_{\rm tot}$	total charge in the oxide layer
r	reflectance
$R_{\rm s}$	surface recombination rate
s	probe spacing
$S_{\rm eff}$	surface recombination velocity
T	absolute temperature [K]
t	thin film thickness
$t_{\rm ox}$	oxide thickness
$t_{\rm trans}$	transmittance
V	voltage
$V_{\rm CPD}^{\rm dark}$	contact potential difference in the dark
$V_{\rm CPD}^{\rm ill}$	contact potential difference under strong illumination
$V_{\rm FB}$	flat band voltage
$V_{\rm m}$	voltage at maximum power point
$V_{\rm oc}$	open-circuit voltage
$V_{\rm ox}$	voltage drop across the oxide layer
$V_{\rm sb}$	surface barrier
W	wafer thickness
ϵ_0	vacuum permittivity
$\epsilon_{\rm r}$	relative permittivity
η	solar cell efficiency
$\mu_{\rm e,h}$	electron/hole mobility
$\nu_{\rm th}$	thermal velocity of charge carriers
ρ	resistivity
σ	conductance
$\sigma_{\rm ns}$	electron capture cross-section
$\sigma_{\rm ps}$	hole capture cross-section
τ	minority carrier lifetime
$\tau_{\rm Auger}$	minority carrier lifetime determined by Auger recombination
$\tau_{\rm bulk}$	minority carrier lifetime in the bulk
$\tau_{\rm e/h}$	electron/hole lifetime
$\tau_{\rm eff}$	effective lifetime
$\tau_{\rm eff,QSSPC}$	effective lifetime determined by the QSSPC method
$\tau_{\rm eff,trans}$	effective lifetime determined by the transient PCD method
$\tau_{\rm rad}$	minority carrier lifetime determined by radiative recombination
$\tau_{\rm SRH}$	minority carrier lifetime determined by Shockley-Read-Hall recombination
$\tau_{\rm surface}$	minority carrier lifetime at the surface
$\phi_{\rm ms}$	work function difference between metal electrode and silicon substrate

Abbreviations

Al_2O_3	aluminium oxide
ALD	atomic layer deposition
AR	anti-reflection
b-Si	black silicon
BSOE	black silicon on emitter
C–V	capacitance–voltage
COCOS	corona oxide characterization of semiconductors
CZ-Si	silicon grown by the czochralski method
CVD	chemical vapor deposition
DC	direct current
DRIE	deep reactive ion etching
ECV	electrochemical capacitance–voltage
FZ-Si	silicon grown by the float-zone method
F^*	fluorine radical
GPC	growth per cycle
H_2	hydrogen (gas)
HCl	hydrogen chloride
H_2O	dihydrogen monoxide
H_2O_2	hydrogen peroxide
HF	hydrogen fluoride
IQE	internal quantum efficiency
KOH	potassium hydroxide
mc-Si	multicrystalline silicon
NaOH	sodium hydroxide
O_2	oxygen (gas)
O^*	oxygen radical
P	phosphorus
PCD	photoconductance decay
PEALD	plasma-enhanced atomic layer deposition
PECVD	plasma-enhanced chemical vapor deposition
$POCl_3$	phosphorus oxychloride
PSG	phosphosilicate glass
PV	photovoltaic
QSSPC	quasi-steady-state photoconductance
RF	radio frequency
RIE	reactive ion etching
SC1/2	standard cleaning 1/2
SEM	scanning electron microscope
SF_6	sulphur hexafluoride
Si	silicon
SIMS	secondary ion mass spectroscopy
SiN_x	silicon nitride
SiO_2	silicon dioxide

SiO_xF_y	silicon oxyfluoride
SRH	Shockley-Read-Hall
SRV	surface recombination velocity
TDMAT	tetrakis(dimethylamino)titanium
TiO_2	titanium oxide
TMA	trimethylaluminium

1 Introduction

Global energy consumption constantly increases. On the other hand, awareness of global warming and the ever tightening CO_2 emission regulations put pressure on states and companies to invest in environmentally friendly resources. Energy from the sun has already been utilized for a long time as heat and as the origin of other indirect energy sources, such as wind power. The amount of solar energy reaching the Earth annually is twice the amount of all fossil resources existing in our planet combined [1]. Thus, the amount of solar radiation arriving onto the Earth's surface is tremendous. Although utilization of solar energy is no longer characteristic of pocket calculators alone, but large solar power plants have been established at several locations, only a small portion of the energy potential of the sun is currently utilized. The main reason hindering the final breakthrough of solar power is the higher price per produced kilowatt hour compared to some other forms of energy. Thus, all new technologies and innovations which enable more efficient and economical utilization of solar energy are of interest of industry as well as of academia.

The most obvious way to reduce the cost of solar power is to improve the actual device where the energy conversion takes place. This device is called a solar cell which converts light directly into electricity based on the photovoltaic effect. When light is absorbed in a material, electrons and holes are generated. These charge carriers are separated by an electric field and subsequently collected at the metal contacts. The field is generated by a p-n junction which is formed by doping heavily a thin layer of the substrate near the cell surface. The dopants are chosen so that the polarity of the heavily doped layer, which is called an emitter, changes its type to opposite to that of the substrate. The emitter also has another important function in the operation of a solar cell: the heavy doping at the metal–semiconductor interface ensures low contact resistance and hence reduces ohmic losses [2]. Since most of the incident light is absorbed near the cell front surface [3], the properties of the emitter region and the surface are of high importance.

In addition to the optimization of the emitter, it is important to minimize reflection losses. Ideally, every incident photon is converted into an electron–hole pair and contributes to the amount of produced electric power. However, reflections from the cell front surface reduce the amount of light entering the device significantly. Therefore, the reflectivity has to be reduced in order to enable high efficiency solar cells. Typically, this is obtained by surface texturing and anti-reflection (AR) coatings, which suppress the reflections efficiently at a certain wavelength [2]. However, these techniques can be optimized only for a narrow wavelength and incidence angle range, which is a clear disadvantage as sunlight consists of various wavelengths and arrives to the cell surface from different angles depending on the time of the day and year.

The limited anti-reflection properties can be overcome by so-called black silicon (b-Si, also called nanograss, nanoporous silicon, etc.), i.e. by nanostructuring the silicon surface. This nanoscale texturization is a promising technology for solar cells since it provides excellent light absorption throughout the whole visible spectrum and for a wide range of incidence angles [4, 5]. However, the enlarged surface area

increases the amount of surface recombination [6], which reduces the cell efficiency, and for a long time the benefit obtained from the reduced reflectivity was overridden by the increased surface recombination losses.

As a solution for the problem of enhanced surface recombination, deposition of an ultrathin film of aluminium oxide (Al_2O_3) with atomic layer deposition (ALD) has been suggested [7, 8]. Effective surface passivation by ALD Al_2O_3 is related to a high density of negative charge in the thin film in addition to good interface quality between the deposited layer and the silicon substrate. Since the polarity of the fixed charge in the film is negative, ALD Al_2O_3 is a suitable material for the passivation of surfaces where electrons are minority carriers, e.g. surfaces doped with boron [9]. Therefore, passivation quality provided by Al_2O_3 on n-type surfaces (often consist of phosphorus emitter), which currently dominate the photovoltaic industry [10], is limited [11].

The goal of this thesis is to address the above problem and find a material with positive fixed charge and low interface defect density on silicon and demonstrate experimentally its passivation efficiency on b-Si n-type emitters. Gas phase phosphorus diffusion is selected as the method for emitter formation in this work as it is widely used in photovoltaic industry. A detailed study on emitter formation in b-Si is left out of the scope of this thesis since the optimization of the diffusion process could be a topic of an entire work by itself. Thus, this work focuses on surface passivation aspects only. Nevertheless, since it is usually challenging to distinguish between recombination at the surface and in the emitter, two different emitter profiles are applied in order to observe the effect of different doping concentration on passivation. ALD is selected as the thin film deposition method as it is capable of providing conformal surface coverage on nanoscale structures [12]. Based on a literature review performed as a part of this thesis, the most promising passivation scheme, SiO_2/Al_2O_3 stacks, is selected and studied experimentally with minority carrier lifetime and contactless C–V measurements. These characterization methods are selected in this study as they provide all the information necessary to determine the charge and interface defect density and the resulting passivation efficiency.

This thesis is divided into five sections. First, theory necessary to understand the studied topic is introduced, including essential basic concepts such as minority carrier lifetime and surface passivation as well as general properties of black silicon. In addition, previous studies regarding b-Si phosphorus emitter passivation and potential thin film materials for that purpose are reviewed. In the third section, physical principles and phenomena, on which the applied characterization methods, such as lifetime and contactless C–V measurements, underlie, are discussed. Process details of the experimental study and obtained results are presented and discussed in Section 4. Finally, conclusions are drawn in Section 5.

2 Theory and background

2.1 Operating principle of a solar cell

Solar cell is a semiconductor component which converts light into electricity. The operation of a solar cell is based on a p–n junction. As p-type semiconductor material with excess holes is brought into contact with n-type material with excess electrons, concentration gradient of charge carriers induces electrons to diffuse from the n-type region into the p-type region and for holes vice versa. As a consequence, positive dopant ion cores in the n-type region and negative ion cores in the p-type region cause an electric field over the junction. This field generates drift currents of charge carriers to direction opposite to the diffusion currents. Consequently, an equilibrium condition is achieved and so-called depletion region with no free charge carriers is formed near the junction, since carriers are rapidly swept from that region by the internal electric field. [2]

The equilibrium can be disrupted by a bias voltage. When a voltage V is applied over the junction, a current can flow through the depletion region. Bias voltage V and the corresponding current I are related to each other by the diode equation:

$$I = I_0 \left(e^{\frac{qV}{kT}} - 1 \right) , \tag{1}$$

where I_0 is the saturation current, q is the elementary charge, k is the Boltzmann constant and T is the absolute temperature in Kelvin. The saturation current is related to the diffusion of minority carriers to the depletion region and can be calculated by formula:

$$I_0 = Aqn_{\mathrm{i}}^2 \left(\frac{\sqrt{D_{\mathrm{h}}/\tau_{\mathrm{h}}}}{N_{\mathrm{D}}} + \frac{\sqrt{D_{\mathrm{e}}/\tau_{\mathrm{e}}}}{N_{\mathrm{A}}} \right) , \tag{2}$$

where A is the area of the junction, n_{i} is the intrinsic carrier concentration, D_{h} and D_{e} are the diffusivities of the minority carriers, τ_{h} and τ_{e} are the hole and electron lifetimes, respectively, and N_{D} and N_{A} are the donor and acceptor densities, respectively. [2]

When a solar cell is illuminated, electron–hole pairs are generated by the energy of the incident photons. These charge carriers diffuse to the p–n junction and are separated by the internal electric field, as shown in a cross-sectional sketch of a solar cell structure in Fig. 1a. Electrons and holes are subsequently collected at the front and back contacts. As the contacts are then connected via an external circuit, the transformed energy can be utilized. Under illumination, the diode equation (Eq. 1) is modified by a term corresponding to the light-generated current I_{L} to give the solar cell current–voltage characteristics:

$$I = I_0 \left(e^{\frac{qV}{kT}} - 1 \right) - I_{\mathrm{L}} . \tag{3}$$

As can be seen from Fig. 1b, the shape of the illuminated and dark characteristic are similar but the former is shifted down by the current I_L. Operating conditions

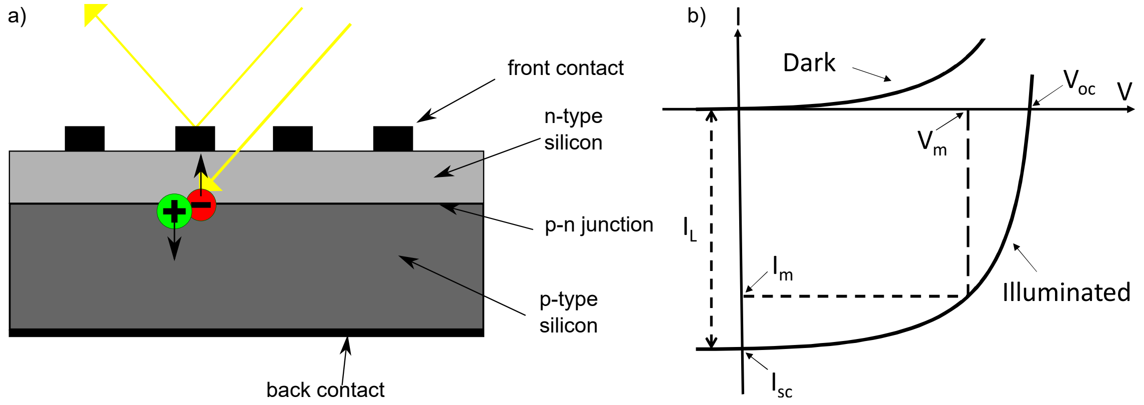

Figure 1: a) Cross-sectional sketch of a solar cell. In addition, generation of an electron–hole pair by light illumination and the separation of charge carriers by an internal electric field are represented. b) Current–voltage characteristics of a solar cell in dark and under illumination. Important quantities, including open-circuit voltage, short-circuit current and the point corresponding the maximum power are highlighted.

within the fourth quadrant of the I–V curve allow power to be extracted from the cell. [2]

The performance of a solar cell is usually characterized by three quantities: short-circuit current I_{sc}, open-circuit voltage V_{oc} and fill factor FF. The short-circuit current flows through a short-circuited cell, while the voltage over the device is zero. Thus, based on Eq. 3, I_{sc} ideally equals the light-generated current. The open-circuit voltage is measured under the opposite conditions, i.e. when the current is zero. By setting this condition into Eq. 3, the following formula can be derived for V_{oc}:

$$V_{\mathrm{oc}} = \frac{kT}{q} \ln \left(\frac{I_{\mathrm{L}}}{I_0} + 1 \right) . \tag{4}$$

For any operating point in the fourth quadrant of the I–V characteristics, the extracted power equals the area of a rectangle shown in Fig. 1b. A certain operating point $(I_{\mathrm{m}}, V_{\mathrm{m}})$ producing the maximum power exists for every cell. The third quantity, fill factor, is the ratio of that maximum power and the theoretical maximum power, which is a product of I_{sc} and V_{oc}, i.e.

$$FF = \frac{I_{\mathrm{m}} V_{\mathrm{m}}}{I_{\mathrm{sc}} V_{\mathrm{oc}}} . \tag{5}$$

In other words, fill factor is a measure of squareness of the I–V curve. [2]

The energy conversion efficiency η, which is the most important quantity of merit of a solar cell, can be calculated from the three quantities introduced above:

$$\eta = \frac{I_{\mathrm{m}} V_{\mathrm{m}}}{P_{\mathrm{in}}} = \frac{I_{\mathrm{sc}} V_{\mathrm{oc}} FF}{P_{\mathrm{in}}} , \tag{6}$$

where P_{in} is the total power of the incident light. Thus, I_{sc}, V_{oc} and fill factor should be as high as possible in order to achieve high efficiency. As can be seen

from Eq. 4, high V_{oc} requires low saturation current, which is mainly limited by recombination losses. Fill factor, on the other hand, is affected by resistive losses. In addition to the reduction of these electrical loss mechanisms, the efficiency can be increased by decreasing optical losses. This includes optimization of the front contact grid to minimize the area blocked by metal contacts and the reduction of surface reflectance. [2]

2.2 Minority carrier lifetime and recombination

As described in the previous section, the separation of light-generated charge carriers by a p–n junction is an essential phase in the solar cell power extraction process. However, before the carriers can be separated, they have to diffuse the whole distance from the position, where they are generated, until to the junction. The average distance which carriers can diffuse in a semiconducting material before they recombine, called diffusion length L, is directly related to the minority carrier recombination lifetime τ in the material:

$$L = \sqrt{D\tau}\,, \tag{7}$$

where D is the diffusivity. Carrier lifetime describes the time the charge carriers are at the excited state on average after the electron–hole pair generation before they recombine. Thus, lifetime is a merit of material quality and ultimately determines the potential of a final solar cell. If the bulk material has low lifetime, the efficiency of a finished solar cell will be poor despite how advanced the cell otherwise is. [2]

2.2.1 Bulk recombination

Three main recombination mechanisms which determine the lifetime in bulk material are radiative recombination, Shockley-Read-Hall [13, 14] recombination and Auger recombination. The processes are shown schematically in Figure 2a-c. These mechanisms are characterized by the corresponding lifetimes: τ_{rad}, τ_{SRH} and τ_{Auger}, respectively, and they all contribute to bulk lifetime τ_{bulk} which can be expressed as the inverse sum of the three components: [15]

$$\frac{1}{\tau_{\mathrm{bulk}}} = \frac{1}{\tau_{\mathrm{rad}}} + \frac{1}{\tau_{\mathrm{SRH}}} + \frac{1}{\tau_{\mathrm{Auger}}}\,. \tag{8}$$

Radiative, or band-to-band, recombination is the inverse phenomenon to electron–hole pair generation. An electron that has been excited to the conduction band returns directly to the valence band and combines with a hole, as shown in Fig. 2a. Simultaneously, a photon with an energy corresponding to the band gap energy is emitted. Radiative recombination rate is directly proportional to carrier density, since the process requires both free electrons and holes to be present simultaneously. Radiative lifetime can thus be represented in the case of p-type substrate as [16]

$$\tau_{\mathrm{rad}} = \frac{1}{B(p_0 + n_0 + \Delta n)}\,, \tag{9}$$

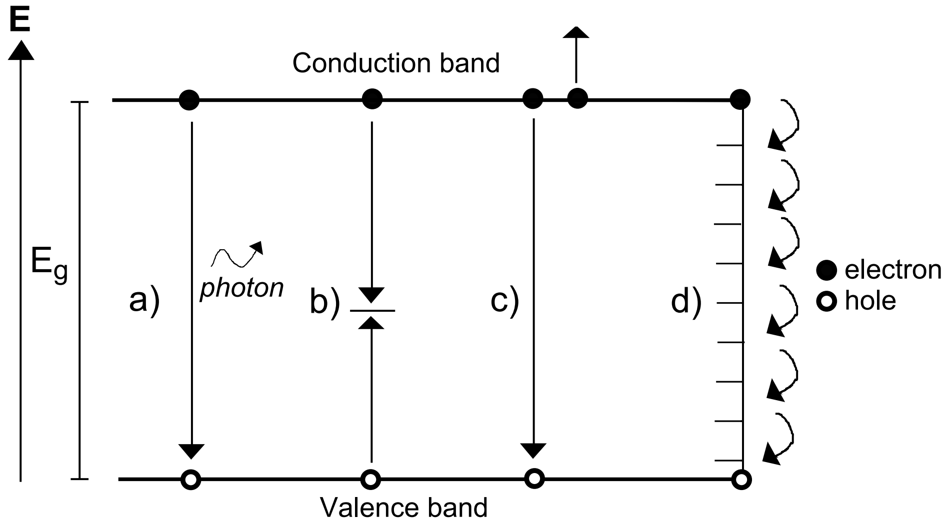

Figure 2: Different recombination mechanisms: a) Radiative recombination, b) SRH recombination, c) Auger recombination, and d) Recombination through surface states

where B is the radiative recombination coefficient, p_0 and n_0 are the equilibrium hole and electron densities, respectively, and $\Delta n = n - n_0 = p - p_0$ is the excess minority carrier density. Radiative recombination occurs rapidly in direct band gap semiconductors and is utilized e.g. in light-emitting diodes to produce light, but is negligibly slow process in materials with an indirect band gap. Since silicon is an indirect band gap material, the effect of radiative recombination can usually be neglected in silicon-based photovoltaic devices [2].

Defects in the crystal lattice introduce energy states in the forbidden band gap. These defects can be e.g. unwanted impurity atoms, crystal damage caused by ion bombardment or intentionally introduced dopants. Charge carriers can recombine through trap-levels introduced by the defects, as shown in Fig. 2b, and the recombination energy is released in the form of phonons, i.e. lattice vibration. [15] This process is called Shockley-Read-Hall (SRH) or multiphonon recombination and the rate is directly proportional to the defect density and carrier concentration of the material [13, 17]. Therefore, SRH recombination is a good merit of material purity and can be reduced by controlling the quality and cleanliness of the semiconductor material during various process steps. Carriers transfer into energy levels in the band gap with a rate which depends on the distance between the introduced level and the band edges. If an electron is transferred into a level near the conduction band edge, it will return more rapidly back to the band than a hole is excited from the valence band into the same state, and recombination is improbable. A corresponding situation, but with opposite charge carriers, concerns states slightly above the valence band edge. Therefore, especially energy states near the mid-gap are effective recombination centers. [15]

The third recombination mechanism in bulk material is Auger recombination. In this process, an electron and a hole recombine and the released energy is absorbed by a third charge carrier which is exited to a higher energy level, as illustrated in Fig.

2c. Charge carriers involved in the process are assumed to be non-interacting particles. As a consequence, Auger lifetime can be approximated under high-injection conditions as:

$$\tau_{\text{Auger,hi}} = \frac{1}{(C_\text{n} + C_\text{p})\Delta n^2}, \tag{10}$$

where C_p and C_n are the Auger recombination coefficients for holes and electrons, respectively. For low-injection conditions, corresponding expressions for n- and p-type silicon are:

$$\tau_{\text{Auger,li}} = \frac{1}{C_\text{n} N_\text{dop}^2} \quad \text{and} \quad \tau_{\text{Auger,li}} = \frac{1}{C_\text{p} N_\text{dop}^2}\ , \tag{11}$$

respectively, where N_dop is the net dopant concentration. Since the Auger lifetime is inversely proportional to the square of the carrier concentration, Auger recombination is most significant at high carrier concentrations, which can be caused by either heavy doping of the material or high-level injection e.g. under sunlight. This is in accordance with the fact that Auger recombination involves three charge carriers, i.e. the more charge carriers are present, the more likely an additional carrier will absorb the released energy. [17]

As a conclusion, in an indirect band gap material, such as silicon, lifetime is limited by SRH recombination at low carrier densities and by Auger recombination at high densities. Whereas the SRH lifetime can be increased by reducing the amount of defects, i.e. by the use of high quality materials and controlling the cleanliness, the Auger lifetime is an intrinsic property of the material and determined by the carrier concentration. [15] These characteristics have to be taken into account in the design of solar cell emitters and the manufacturing process.

2.2.2 Surface recombination

A periodic crystal lattice is abruptly disrupted at material surfaces. Since the semiconductor atoms at the surface lack one or more neighbouring atoms, they cannot form as many bonds with other atoms as those in the middle of the lattice. As a consequence, the surface contains non-saturated, so-called dangling bonds which induce allowed energy states in the band gap and act as effective trap sites for SRH recombination, as shown in Fig. 2d. Since a large portion of the incoming photons with short wavelengths are absorbed near the solar cell surface, surface recombination is a significant source of recombination in those devices and has to be considered in the design of the device. [18]

Surface SRH recombination rate R_s via a surface state at an energy E_t is given by [14]

$$R_\text{s} = \frac{\sigma_\text{ns}\sigma_\text{ps}\nu_\text{th}N_\text{it}(n_\text{s}p_\text{s} - n_\text{i}^2)}{\sigma_\text{ns}(n_\text{s} + n_\text{1s}) + \sigma_\text{ps}(p_\text{s} + p_\text{1s})}\ , \tag{12}$$

where ν_th is the thermal velocity of charge carriers (approximately 10^7 cm/s at room temperature [18]), n_i is the intrinsic carrier concentration in the material, N_it is the surface or interface defect density (unit: cm^{-2}), σ_ns and σ_ps and n_s and p_s

are the electron and hole capture cross-sections and concentrations at the surface, respectively, and

$$n_{1\mathrm{s}} = n_\mathrm{i} \cdot \exp\left(\frac{E_\mathrm{t} - E_\mathrm{i}}{kT}\right) \quad \text{and} \quad p_{1\mathrm{s}} = n_\mathrm{i} \cdot \exp\left(-\frac{E_\mathrm{t} - E_\mathrm{i}}{kT}\right) , \tag{13}$$

where E_i is the intrinsic Fermi energy, k is the Boltzmann constant and T is the absolute temperature. The ν_th dependence of R_s originates from the fact that the diffusivity of the material ultimately limits the maximum amount of surface recombination, since the carriers cannot recombine at the surface more rapidly than they diffuse to it from the bulk. [2] In Eq. 12, N_it is assumed to be constant. However, if that is not the case, the energy-dependent interface defect density D_it (unit: $\mathrm{cm^{-2}eV^{-1}}$) has to be integrated over energy [15].

As can be seen from Eq. 12, the surface recombination rate is directly proportional to the amount of interface defects, including dangling bonds, at the surface. Thus, the number of surface states has to be reduced in order to prevent charge carriers from recombining at the surfaces. In addition, the larger the surface area, the more possible places for dangling bonds exist, i.e. a larger surface area promotes surface recombination. Since the SRH recombination process involves one charge carrier of both types, i.e. an electron and a hole [14], the surface recombination rate is at its maximum when the surface concentrations of electrons and holes are equal. Thus, the rate depends also on the carrier concentrations and the injection level. Methods to control the amount of surface recombination are discussed more thoroughly in Section 2.3.

It is usually difficult to distinguish between bulk and surface recombination by experimental methods. Therefore, the measured lifetime involves their combined effect and is usually called effective lifetime, τ_eff, which can be expressed as [15]

$$\frac{1}{\tau_\mathrm{eff}} = \frac{1}{\tau_\mathrm{bulk}} + \frac{1}{\tau_\mathrm{surface}} . \tag{14}$$

The rate of surface recombination is usually reported in the form of surface recombination velocity (SRV) instead of the corresponding lifetime. When the front and back surfaces are assumed to be identical, SRV, or S_eff, can be approximated from the measured effective lifetime by [19]

$$S_\mathrm{eff} = \frac{W}{2}\left(\frac{1}{\tau_\mathrm{eff}} - \frac{1}{\tau_\mathrm{bulk}}\right) , \tag{15}$$

where W is the wafer thickness. Thus, SRV is inversely proportional to the effective lifetime, i.e. the shorter the lifetime, the higher the velocity. In addition, if the bulk lifetime is approximated to be infinite, i.e. the material is assumed to be free of defects and of high quality, Eq. 15 is reduced to give the maximum value of SRV:

$$S_\mathrm{eff,max} = \frac{W}{2 \cdot \tau_\mathrm{eff}} . \tag{16}$$

2.3 Surface passivation

Since wafer surfaces are a major source of recombination in solar cells and other semiconductor devices, reduction of surface recombination is important. This can be achieved by so-called surface passivation. Eq. 12 suggests two different means for reducing the surface recombination rate: the reduction of surface state density, N_{it} or D_{it}, and the reduction of the product of surface carrier concentrations, $n_{\mathrm{s}}p_{\mathrm{s}}$. The former is called chemical passivation and the latter field-effect passivation. [20]

According to Eq. 12, the surface recombination rate is proportional to surface defect density. Thus, the surface recombination is drastically reduced when the amount of surface states is decreased. This can be achieved by depositing a thin film on top of a wafer surface. Silicon atoms at the surface form bonds with the atoms in the deposited film and the amount of dangling bonds is hence reduced. [20]

As already mentioned in Section 2.2.2, SRV depends on the surface carrier concentration of both electrons and holes. The product $n_{\mathrm{s}}p_{\mathrm{s}}$ can be substantially reduced if the surface is depleted from one type of charge carriers. More effective passivation can usually be obtained by decreasing the surface concentration of minority carriers since their density is initially smaller. As electrons and holes have an electric charge, they can be repelled from the surface with an electric field. The field can be induced by a p–n junction below the surface, by a gate voltage or by charges in an insulating layer deposited on top of the surface [20]. Since charges with the same polarity repel each other, either electrons or holes are repelled from the surface depending on the polarity of the charges in the deposited thin film, and the ones with the opposite polarity are attracted towards it.

Different field-effect passivation schemes with a negative-charge thin film, e.g. an oxide, are represented in Fig. 3a-d. As SRH recombination process always requires one charge carrier of either type and the minority carriers (i.e. electrons in the case of a p-type substrate) are repelled from the surface, whereas the majority carriers (i.e. holes) are attracted close to it (Fig. 3a), the surface recombination rate is reduced drastically. Effective passivation can be achieved also in the case of n-type surfaces where holes are the minority carriers. If the charge density in the thin film is high enough and the substrate only lightly doped, a thin layer of silicon right below the surface turns into p-type, i.e. the hole concentration becomes higher than that of electrons, as shown in Fig. 3b [21]. Thus, so-called inversion condition is achieved and, as a consequence, surface recombination rate is again reduced. However, if the charge density in the film is low or the substrate heavily doped, the carrier densities become more equal and surface recombination is actually enhanced.

The polarity of the fixed charge has more significance in the case of highly doped surfaces. The negative charge is suitable for passivation of p+ surfaces, since the surface is again depleted from electrons by the electric field generated by the negative charges (Fig. 3c). However, the inversion condition required for efficient field-effect passivation of n-type surfaces cannot be achieved if the surface doping concentration is very high, since the carrier density difference is initially too large. Therefore, the negative charge is in general detrimental for n+ surface passivation (Fig. 3d) [11,22].

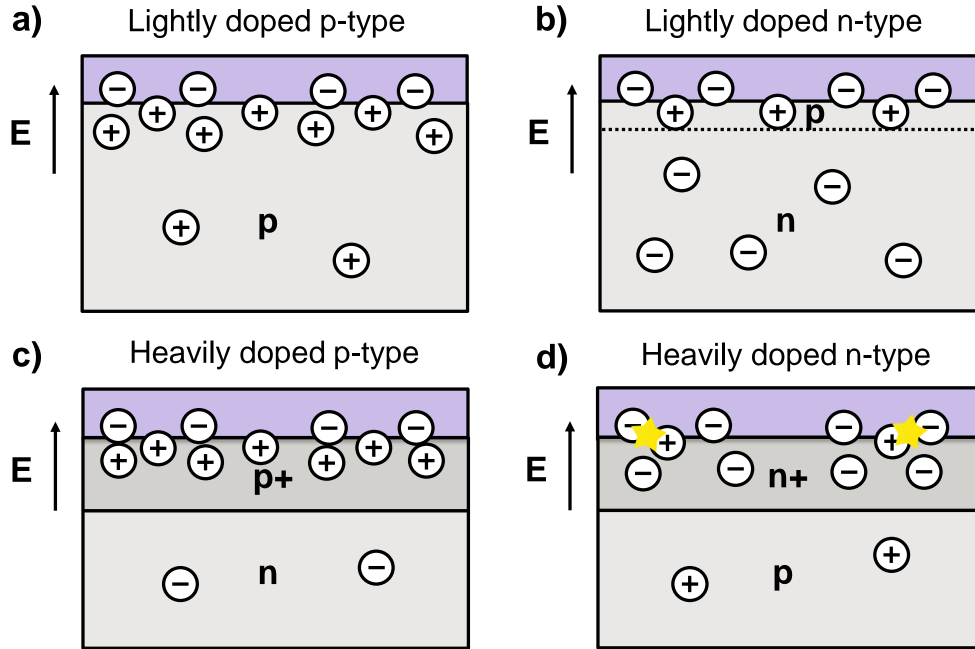

Figure 3: Different field-effect passivation schemes with a negative-charge thin film: a) Lightly doped p-type wafer is effectively passivated since the surface is depleted from electrons. b) An inversion layer is formed at the surface of a lightly doped n-type wafer. c) Negative oxide charges work also in the case of heavily doped p+ surface. d) On heavily doped n+ surface, the negative charge is detrimental for surface passivation as it attracts the minority carriers to the surface.

2.3.1 Oxide charge

In the example above, an oxide with negative charge was considered. Oxide charges can be divided into four different types: interface or oxide trapped charges and fixed or mobile oxide charges [15].

Interface trapped charges, Q_{it}, are located at the interface of silicon and the oxide layer. They are due to defects or impurities at a material interface. These charges are in electrical contact with the underlying silicon and can be charged or discharged depending on the surface potential. The quantity of Q_{it} depends on the interface defect density, D_{it}, which is a good merit of interface quality and can usually be reduced by post-deposition annealing of the film. Fixed oxide charge, Q_{f}, is also located near the interface, but is not in electric connection with silicon. The amount of fixed charges usually depends on the growth conditions and subsequent process steps. Oxide trapped charges, Q_{ot}, are electrons and holes trapped in the oxide layer as a result of e.g. tunneling, ionizing radiation or avalanche injection. Thus, charge can become trapped in the oxide also during device operation, not only during the fabrication process. Q_{ot} is usually distributed through the oxide layer, contrary to fixed charge. Mobile oxide charges, Q_{m}, are due to ionic impurities in the oxide and they can move within the thin film depending on the electric field applied over the oxide. [15]

Although electrons and holes are affected by electrostatic forces caused by all types of charges, the most important type concerning field-effect passivation is the fixed charge due to two reasons. First, these charges are not affected by an applied voltage and second, since they are located near the silicon surface, the Coulomb interaction is strong. Therefore, study on oxide charges with respect to surface passivation usually concentrates on fixed charge densities.

2.4 Black silicon

2.4.1 Optical properties

As described in Section 2.1, one way to increase solar cell efficiency is to reduce optical losses. Only photons which are absorbed can create electron-hole pairs and hence produce energy in solar cells. The absorptance a is related to reflectance r and transmittance t_{trans} as

$$a = 1 - r - t_{\text{trans}} \,. \tag{17}$$

Thus, in order to increase the absorption, reflectance and transmittance have to be reduced. The reflectivity of a polished silicon surface is around 40 % [23]. Therefore, without any operations towards a lower reflectance, nearly half of the incident light will be lost already at the front surface of the solar cell. Since as large portion of the incident light as possible needs to be absorbed, the front surface is usually covered with an anti-reflection (AR) coating. In addition, surface texturing is used to reduce the reflectance in high-efficiency solar cells. The surface is roughened, in which case a reflected light ray has a higher probability to bounce back onto the surface. Random or inverted pyramids (Fig. 4a), whose fabrication is based on crystal orientation dependent wet etching of silicon in potassium hydroxide (KOH) or sodium hydroxide (NaOH) based solutions, are examples of surface texturing that are used in solar cell industry. Although textured surfaces reduce the reflectance down to several percent, the use of AR coatings is usually required with them in order to achieve high efficiency. In addition, these techniques can be optimized only for a narrow wavelength range. [2]

Unlike random pyramids, which have dimensions larger than the wavelength of light, the use of so-called black silicon eliminates the requirement of AR coatings. The name originates from the fact that the reflectance of black silicon is so low that it appears black to a naked eye. The structure consists of nanosized silicon spikes with dimensions smaller than the wavelength of the incident light, as shown in Fig. 4b. Consequently, the surface appears to light as a homogeneous medium with a smoothly increasing density [5]. Based on the electromagnetic wave theory, reflection may occur when light encounters a boundary of two materials with different refractive indices [26]. Since at air–b-Si interface the refractive index changes smoothly from one of air to 3.88 of silicon (at 632.8 nm wavelength) [3], negligible reflections occur. Reflectance of b-Si and inverted pyramid textured surfaces as a function of wavelength are shown in Fig. 5. As can be seen, b-Si provides low reflectance over the entire visible spectrum, whereas the reflectance of the inverted pyramids increases radically in the ultraviolet wavelength range, despite the deposited AR

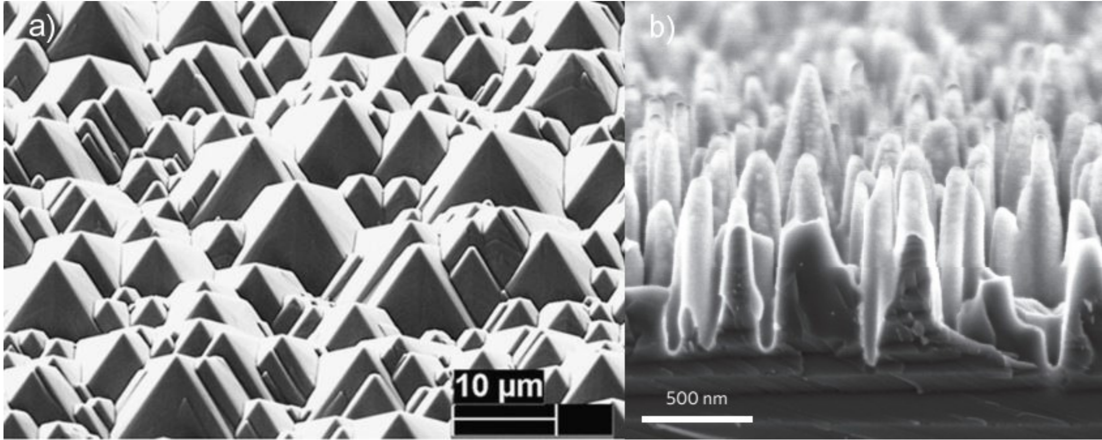

Figure 4: Surface structures used to reduce reflectance: a) random pyramids produced by wet chemical etching [24] and b) b-Si fabricated by cryogenic DRIE [25]. Note the different scales in the figures.

coating. In addition, the absorbance of b-Si decreases less than 1 % compared to normal incidence for incident angles up to 55° [25], whereas AR coatings can be optimized only for a certain incidence angle, typically for perpendicular rays. This is remarkably important for solar cells, since the solar radiation arrives to the surface from different angles depending on the time of the day and the year.

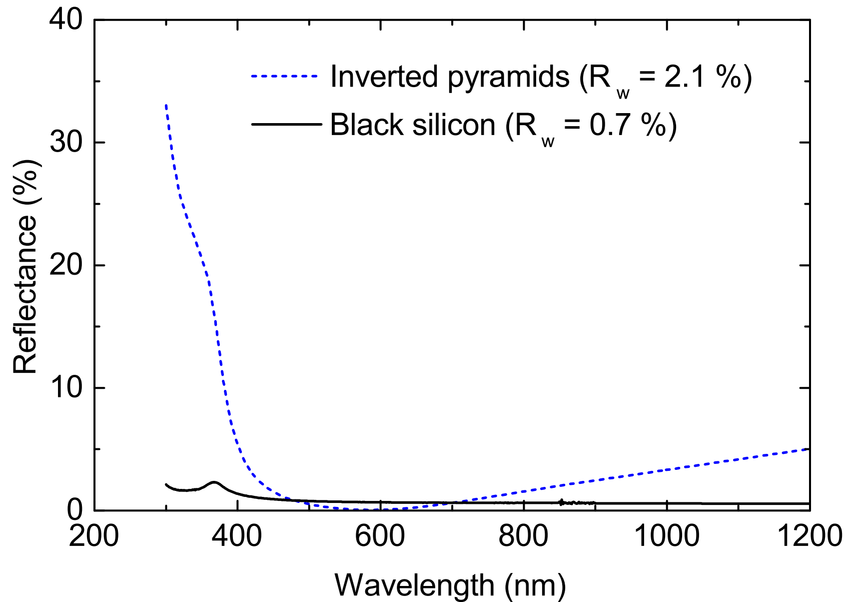

Figure 5: Reflectance of a b-Si surface as a function of wavelength. As a reference, reflectance from inverted pyramids covered with an AR coating is shown. The average reflectance weighted by the solar spectrum is shown in parenthesis. [27]

In addition to low reflectance, b-Si surface scatters light efficiently and hence reduces the transmittance by enhanced light trapping [28]. Since a light ray, which is not reflected, changes its direction at the front surface, the path length it travels

in the bulk material before it may escape the wafer is significantly increased. As a consequence, light is absorbed closer to the surface, which enables more efficient absorption of photons with a longer wavelength and the use of thinner substrates. [2] This is important especially from the cost perspective.

2.4.2 Fabrication

Several different b-Si fabrication methods exist, including metal-assisted wet chemical etching [29], laser treatment [30] and reactive ion etching (RIE) with predeposited nanoparticles as masks [31]. One of the widely used techniques is maskless cryogenic deep reactive ion etching (DRIE). Black silicon was originally an unwanted side product of DRIE to determine suitable process conditions for etching vertical walls in silicon [32]. Two process gases, SF_6 and O_2, are introduced into the chamber simultaneously. SF_6 provides F^*-radicals which etch silicon chemically, and O_2 produces O^*-radicals which form a passivating SiO_xF_y layer. As a consequence, a constant competition between etching and passivation exists. A cryogenic temperature is needed since the reaction products are volatile in temperatures higher than approximately $-100°C$ [33].

The increase of SF_6 content results in pronounced etching and thus more isotropic profiles, whereas a larger concentration of O_2 enhances the passivation. Since directional ion bombardment removes the oxide layer from horizontal surfaces, etching proceeds to vertical direction under suitable process conditions. Excessive amount of oxygen results in a situation where residues of the passivation layer remain on the surface at random positions and act as micromasks. As the etching process continues, nanospikes, i.e. black silicon, are formed. [34] The morphology of the b-Si structure can be modified by varying the process parameters, such as SF_6/O_2 flow ratio, chamber pressure, RF power and temperature [35].

2.4.3 Electrical properties

One of the major challenges in the utilization of b-Si for photovoltaic applications is the enhanced surface recombination since, as discussed in Section 2.2.2, a large surface area induces an increased surface recombination rate. Surface recombination velocity has been proven to be inversely proportional to the square of the charge density at the Si surface on planar wafers [36]. However, a corresponding proportionality to the fourth power was observed on b-Si, and hence a higher charge density is required for efficient passivation of b-Si surfaces [8].

As the deposited thin films follow the nanostructured surfaces, a larger relative charge density surrounds the silicon in the needles compared to planar surfaces, as shown schematically in Fig. 6 in the case of negative-charge Al_2O_3. Therefore, a substantially larger effective charge density is usually measured on b-Si surfaces. The ratio between the charge densities on b-Si and planar surfaces has been found to equal the corresponding surface area ratio [8]. Similar effect of the enhanced surface area has been observed in the case of doping of nanostructured surfaces which will be discussed in Section 2.5.1.

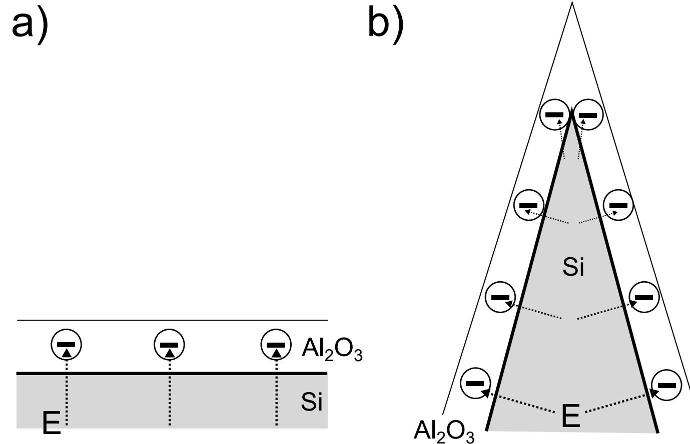

Figure 6: Electric field induced by fixed charges in Al_2O_3 in a) planar and b) b-Si surface. Larger charge density is measured in the case of a nanostructured surface since the needles are surrounded by the thin film.

2.5 Solar cell emitter

In silicon solar cells, the p–n junction is usually formed by introducing a high concentration of dopants into the material near the wafer surface. This so-called emitter region is typically fabricated by ion implantation or solid or gas phase diffusion. In ion implantation, ions with high energy are shot onto the semiconductor surface, and the wafer is subsequently annealed at high temperature to remove lattice damage induced by the ion bombardment and to activate the dopants. In the diffusion methods, which are more often applied in PV industry, wafers are loaded into a heated furnace, into which e.g. gaseous phosphorus oxychloride ($POCl_3$) is introduced. Phosphorus atoms will react with the Si surface and diffuse deeper into the material due to the high temperature. Ion implantation provides more precise control over the dose and final depth of the dopants. However, due to lower cost and better applicability to high volume mass production, gas phase diffusion is the dominant process used in the photovoltaic industry. [12]

Amount of doping in the emitter layer is usually described by sheet resistance, since it can straightforwardly be measured by a four-point-probe. A current I is passed through two probes, and the induced voltage V is measured with another two probes between the first ones. With equal probe spacing s, the resistivity ρ is given by

$$\rho = 2\pi s \frac{V}{I} \,. \tag{18}$$

The depletion region at the p–n junction acts as an insulator and keeps the current flow in the emitter region. For a uniformly n-doped thin layer, the sheet resistance R_{sheet} is defined as

$$R_{\text{sheet}} = \frac{\rho}{t} = \frac{1}{q\mu_{\text{e}} N_{\text{D}} t} \,, \tag{19}$$

where t is the layer thickness, μ_{e} is the electron mobility and N_{D} is the doping concentration. However, an emitter is never completely uniform in practice and

R_{sheet} is given as an integral over the emitter layer:

$$R_{\text{sheet}} = \frac{1}{\int_0^t \frac{1}{\rho(x)} dx} \,. \tag{20}$$

High sheet resistance inflicts resistive losses and necessitates a short spacing between the front metal contacts, hence reducing the amount of light absorbed in the cell. Sheet resistance can be reduced by doping the emitter as heavily as possible. In addition, the cell surface has to contain enough dopants to ensure low contact resistance. However, too high level of doping in the emitter disrupts the periodic crystal structure which increases the number of effective recombination centers. If the amount of dopants is larger than the solid solubility of the material, the excess atoms will incorporate into precipitates and so-called dead layer may be formed near the surface. In such cases, minority carrier lifetime in the emitter is drastically reduced and most of the charge carriers generated near the front surface will recombine. Moreover, high doping increases Auger recombination, as discussed in Section 2.2, which also reduces the collection probability of charge carriers. Based on this discussion, an optimum emitter doping level exists. Emitter sheet resistivity is typically in the range of 30–100 $\Omega/\square$ in silicon solar cells. [2]

In addition to the amount of dopants, the depth profile of the doping concentration has to be designed carefully. The emitter should be shallow enough to prevent long path lengths for light-generated charge carriers. On the other hand, too shallow an emitter may induce shunting problems. [2]

The performance of an emitter is usually characterized by emitter saturation current density, $J_{0\text{e}}$. It reflects the recombination at the front surface and in the volume of the emitter, including SRH and Auger recombination mechanisms as well as heavy-doping effects such as band gap narrowing and possible dead layers. $J_{0\text{e}}$ is the efficiency-limiting parameter for solar cells with minority carrier diffusion lengths twice the device thickness. If other recombination paths, such as recombination in the space charge region, are present, the measured values represent the maximum emitter saturation current densities. Physical principles of $J_{0\text{e}}$ extraction are discussed in more detail in Section 3.3. [2]

2.5.1 Emitter in black silicon

The enlarged surface area of b-Si introduces more complexity to the design of solar cell emitter. The effect of the nanostructure aspect ratio and the doping concentration of b-Si emitters on effective charge carrier lifetime has been studied in detail e.g. by Oh *et. al.* [6]. Three different doping concentration regimes were distinguished, in which either Auger or surface recombination dominated. Dopant diffusion from the entire surface of the nanostructures resulted in excessive doping compared to planar references. In addition, the phosphorus concentration was discovered to be constant and close to the surface peak concentration throughout the whole nanostructures. This resulted in enhanced Auger recombination with comparatively large doping concentrations. On the other hand, surface recombination was the limiting factor in samples with less doping. Thus, nanostructuring enhanced both Auger and

surface recombination by altering the doping profile and increasing the surface area, respectively. [6]

Based on the identification of different sheet resistance regimes in which different recombination mechanisms dominated, Oh *et. al.* suggested design rules for efficient nanostructured solar cells and fabricated a p-type cell with a phosphorus diffused emitter which reached a high efficiency of 18.2 %. However, their cell suffered from poor blue response in internal quantum efficiency (IQE). This was largely due to a higher doping concentration, and hence pronounced Auger recombination, in b-Si than in planar wafers for the same doping conditions, although this phenomenon is usually associated to the larger surface area itself. Also Yuan *et. al.* [37] observed similar poor blue response in their b-Si solar cells. The nanostructures were fabricated by metal-assisted etching with various aspect ratios and passivated with thermal SiO_2. Based on simulations, the reduction in IQE was explained by an overly doped dead layer in the b-Si structure due to excessive doping through the enlarged surface area. [37] Thus, the blue response could be substantially improved by adjusting the doping conditions to be more appropriate for b-Si instead of utilizing the parameters optimized for planar wafers.

Liu *et. al.* [38] studied the reduction of doping concentration in b-Si by comparing an oxidation process with high pressure and a low temperature (20 atm, 450 °C) to a conventional high-temperature oxidation (1 atm, 800 °C). The low-temperature passivated cell outperformed the high-temperature processed sample especially in the blue wavelength range, which was attributed to the suppression of a dead layer by avoiding high-temperature processes. Phosphorus diffused easily into SiO_2 at a high temperature which resulted in the formation of dead layers in the high-temperature processed samples and hence degraded the cell performance at the short wavelength range. Despite the improvement achieved with a lower process temperature, neither of the b-Si cells could reach the efficiency of a planar reference cell. [38]

None of the above-mentioned studies concentrated on the determination of the actual doping concentration in b-Si, but the enhanced doping was deduced by indirect means, e.g. from a lower sheet resistance and poorer blue response. A comprehensive study on phosphorus emitter formation by $POCl_3$ gas phase diffusion in nanostructured silicon has been performed by Kafle *et. al.* [39]. Based on simulations and confirmed with experimental methods, surfaces of the nanostructures were observed to be extremely heavily doped and the p–n junction to be deeper in the b-Si samples than in wet-chemically textured wafers. The surface doping concentration was reduced by using a lower temperature during the phosphosilicate glass (PSG) deposition resulting in lower P concentration in the glass and by applying a high O_2 flow during a subsequent drive-in step. Despite the structured surface, the p–n junction was revealed to be rather planar below the nanostructures. [39] A similar observation was reported also by Shen *et. al.* in b-Si fabricated with plasma immersion ion implantation [40]. In addition, the doping profile measured from the bottom of the nanostructures followed the profile in a planar sample [39].

2.6 Thin film materials for surface passivation of n+ emitters

2.6.1 Aluminium oxide

Aluminium oxide (Al_2O_3) is the most studied ALD-material to date, especially the deposition process with trimethylaluminium (TMA) and water as precursors. With ALD Al_2O_3, excellent surface passivation has been demonstrated on lightly doped surfaces and boron emitters [41, 42]. The high level of passivation is due to efficient field-effect passivation induced by a high density of negative charge in the thin film [41]. The charge is suggested to originate from electron trapping to O-interstitials or Al vacancies, since they both produce defect states in the Al_2O_3 band gap below mid-gap and can hence be negatively charged [43]. In addition, a tetrahedrally coordinated Al site at the Al_2O_3–Si interface has been proposed [44]. The material provides also good interface quality between the deposited layer and the silicon substrate. Furthermore, Al_2O_3 with a refractive index of 1.65 is transparent to visible light and hence absorbs negligible amount of the incident light [3]. However, the negative charge in Al_2O_3 is detrimental for phosphorus emitter passivation with certain doping densities (sheet resistance ~150 Ω/□), since the minority carriers are attracted to the surface and SRV hence increased, as discussed in Section 2.3 [11,22]. Nevertheless, due to a high level of chemical passivation provided by the thin film, Al_2O_3 has been used to passivate also n+ surfaces in the sheet resistance range of 30–100 Ω/□ [11].

Best results amongst nanostructured solar cells have been achieved with ALD Al_2O_3 [25, 27]. The excellent conformality and the effective field-effect passivation have solved the problem of enhanced surface recombination due to the enlarged surface area [7]. The high density of fixed charge in Al_2O_3 thin films has enabled efficient passivation on both lightly doped p- [7] and n-type [8] b-Si surfaces. Since the charges have negative polarity, ALD Al_2O_3 is highly suitable for the passivation of p+ emitters where electrons are the minority carriers [9].

Wang *et. al.* [45] fabricated an 18.2 % efficient p-type b-Si solar cell by using silver-catalysed wet chemical etching, $POCl_3$ diffusion and ALD Al_2O_3 for producing the nanostructures, emitter formation and surface passivation, respectively. A positive oxide charge appropriate for n+ surface passivation was observed in the as-deposited thin film. However, a rather high D_{it} resulted in only modest increase in the cell performance compared to a reference cell with no surface passivation. The highest efficiency was obtained by forming gas annealing the film which changed the polarity of the oxide charge and reduced the D_{it} substantially. Thus, the improved chemical passivation by the post-deposition annealing was found to be more effective than the field-effect passivation by the appropriate polarity of oxide charge in the as-deposited state. [45]

To be able to benefit also from the field-effect passivation, the same research group studied ALD Al_2O_3/TiO_2 dual-layer passivation with various deposition and annealing schemes on n+ emitters of nanostructured solar cells. All stacks and TiO_2 single layers provided high positive oxide charge densities. However, the interface quality with a bare TiO_2 film was poor despite forming gas annealing. As a consequence, TiO_2 resulted in lower cell efficiencies compared to bare Al_2O_3, in spite

of the negative charge in the latter. Nevertheless, optimal properties for n+ surface passivation were achieved by combining the low D_{it} of Al_2O_3 and the positive charge of TiO_2. With these Al_2O_3/TiO_2 stacks, positive oxide charge densities of $4 \cdot 10^{12}$ cm^{-2} and interface defect densities of $4 \cdot 10^{11}$ cm^{-2}eV^{-1} were obtained, resulting in an 18.5 % efficiency in a b-Si solar cell. [46] However, also contradictory results have been published by e.g. Suh *et. al.* [47]. Similar ALD Al_2O_3/TiO_2 passivation was applied on p+ emitters, and the negative fixed charge density in Al_2O_3 was observed to increase by the TiO_2 capping layer deposition. As a consequence, J_{0e} of p+ emitters was reduced due to enhanced field-effect passivation [47], which indicates that the SRV in the case of n+ emitters would have been deteriorated. These contradictory observations may partly be due to the use of different precursors. While TMA + H_2O were used for Al_2O_3 by both authors, Wang *et. al.* used tetrakis(dimethylamino)titanium (TDMAT) and remote O_2 plasma for TiO_2, whereas Suh *et. al.* applied titanium chloride and H_2O based process.

As a conclusion, a thin film with high conformality, good interface quality and positive charge are required for b-Si solar cells with an n+ emitter, the latter requirement not being fulfilled by ALD Al_2O_3.

2.6.2 Thermal silicon dioxide

Thermal silicon dioxide (SiO_2) has been the traditional material for surface passivation of silicon, since it provides extremely low interface defect density [48] and the growth processes are thoroughly studied due to their development for the IC industry. However, thermally grown silicon dioxide is not the optimum material for surface passivation in all applications. The thermal growth of SiO_2 requires high temperature which has several drawbacks. First, high temperature steps cause dopants to diffuse deeper into the wafer and into the oxide layer, which complicates the design of diffusion profiles of the final device [21]. Furthermore, high temperature can significantly degrade bulk lifetime as impurity atoms, e.g. heavy metal contamination, diffuse deeper into the bulk material. This is a problem especially with multicrystalline silicon (mc-Si), where a considerable amount of impurities exists at grain boundaries. In addition, energy needed for heating the furnaces increases production costs.

Despite the disadvantages, SiO_2 provides excellent chemical passivation especially on high-resistivity n- and p-type substrates, and SRV values below 10 cm/s have been reported [49]. However, the passivation is inefficient on heavily doped p-type surfaces due to a small amount of positive fixed charge in SiO_2 [50]. Phosphorus doped surfaces instead have been passivated with thermal SiO_2. Cuevas *et. al.* [51] fabricated n+ emitters in planar wafers with varying sheet resistances with $POCl_3$ diffusion at 850–900 °C. The surfaces were passivated with 20–50 nm of SiO_2 grown at 900 °C and annealed in nitrogen at the same temperature. A linear correlation between the emitter saturation current density and sheet resistance was observed with J_{0e} values varying between 110 and 10 fA/cm^2 for emitters with sheet resistance of 40–400 Ω/□. [51] Also Kerr *et. al.* [52] passivated phosphorus emitters with varying doping profiles by forming gas annealed thermal oxide. In the sheet

resistance range of 50–200 Ω/□ with electrically active P surface concentration of 1–5 $\cdot 10^{19}$cm^{-3}, J_{0e} was 12–50 fA/cm^2. [52]

Since thermal oxidation provides excellent surface conformality, the process has been employed also for b-Si phosphorus emitter passivation. The topic has been studied by several research groups with different b-Si structures [6, 37, 38, 53, 54]. Although Oh *et. al.* [6] achieved rather high conversion efficiency of 18.2 % with their b-Si solar cell, the SRV was in the range of 150–300 cm/s in shallow to deep nanostructured surfaces due to the lack of proper field-effect passivation. Also large-area b-Si cells fabricated by Yoo *et. al.* [54] resulted in only 11.7 % efficiency, though the cells suffered from other issues as well. In summary, none of the thermal SiO_2 passivated cells has reached as high performance as achieved with ALD Al_2O_3.

2.6.3 Hydrogen-annealed SiO_2

The challenge in surface passivation by thermal SiO_2 is the negligible field-effect passivation provided by a low fixed charge density in the oxide layer. Nevertheless, Vanheusden *et. al.* [55] observed that hydrogen annealing of buried oxide formed by implanted O^+ ions introduced a considerable amount of positive fixed charge in the oxide layer. The authors etched the top silicon layers from some of the samples prior to the annealing process and annealed all samples in 99.9999 % pure H_2 in 1.1 atm pressure at varying temperatures in the range of 223–1050 °C. After the desired time, the samples were cooled to room temperature in an unaltered ambient. The charge densities measured by electron spin resonance method and confirmed by C–V measurements were in the range of $5 \cdot 10^{12}$ cm^{-2}, which are comparable to the negative charge densities measured from ALD Al_2O_3 thin films [36]. Regardless of the removal of the top Si layer, similar behaviour of charge density as a function of the annealing temperature were measured from both sample types. Annealing temperature of 600–700 °C was observed to produce the highest charge. However, a subsequent vacuum annealing at 700 °C removed the charge, which could be restored by another subsequent H_2 annealing. Thus, the annealing did not alter the structure of the oxide in a permanent way. [55]

The positive charge formation was explained by the incorporation of H atoms in strained Si–Si bonds caused by neutral oxygen vacancies present in the buried oxide. Correspondingly, the dissipation of the charged state in vacuum was suggested to occur via the reverse reaction, i.e. the dissociation of the H atoms. Hydrogen annealing at a temperature higher than 715 °C, however, was proposed to activate a stable neutral state at the same site as the positively charged state and hence to prevent the formation of positive charge. A subsequent H_2 annealing in a lower temperature was unable to activate the positive state, as observed experimentally, since the site was already filled. [55]

Afanas'ev *et. al.* [56] studied the same topic with thermally grown oxide layers in addition to buried ones. Both dry and wet oxidation were employed at 700–850 °C and 950–1100 °C with oxide thicknesses between 5 and 410 nm. Thermal oxidation was followed by a post-oxidation annealing, which resulted in an initial positive fixed charge density below $2 \cdot 10^{11}$ cm^{-2}. The samples were subsequently annealed in pure

hydrogen at temperatures between 400 and 800 °C for one hour and cooled rapidly in an unaltered ambient in order to minimize annealing of the positive charge. C–V measurements revealed fixed charge densities up to $1 \cdot 10^{13}\,\mathrm{cm}^{-2}$ in samples annealed in H_2 at 450–670 °C. As in the study by Vanheusden *et. al.* [55], Afanas'ev *et. al.* observed a H_2 annealing at a temperature higher than 700 °C or in vacuum to reduce the amount of positive fixed charge, also in the case of thermal oxide. No considerable dependence on oxide thickness was observed for oxides thicker than 5 nm, which refers to the interfacial nature of the positive charge. In addition, the trend of the oxide charge as a function of the annealing temperature and oxide thickness was discovered to be similar for both thermal and buried oxides. [56] Thus, it can be assumed that also results reported by Vanheusden *et. al.* can be applied to thermal SiO_2, and a high density of positive charge would be expected by annealing silicon dioxide films in hydrogen.

2.6.4 Silicon nitride and amorphous silicon

Silicon nitride (SiN_x) deposited with plasma-enhanced chemical vapor deposition (PECVD) is currently widely used in the photovoltaic industry to passivate phosphorus emitters of p-type solar cells due to the positive fixed charge in the SiN_x thin films [57]. In addition to efficient field-effect passivation and reasonable interface quality, SiN_x provides good antireflection properties, which can be controlled by adjusting the relative concentrations of silicon and nitrogen during the deposition process [58].

Otto [59] compared passivation quality of ALD Al_2O_3 and PECVD SiN_x on various b-Si morphologies. Comparable lifetimes were reported for both schemes on polished samples, whereas the former outperformed the latter on b-Si, particularly on deep nanostructures. The difference in the passivation effectiveness was mainly explained by the inhomogeneity of the SiN_x layer, since PECVD was unable to deposit a conformal film on b-Si. [59] Applied to nanostructured cells, the same phenomenon was observed to result in a low fill factor by Liu *et. al.* [60]. Since AR coatings are not required on high aspect ratio b-Si surfaces, which provide nearly zero reflectance as such [7], SiN_x provides no further advantage in that perspective either. Also several studies regarding nanostructured emitters passivated with SiN_x have been performed [61–63]. However, the reflectance of the inspected surfaces has been in the order of 5–10 % in most publications, and the thin films have simultaneously been utilized as a necessary AR coating.

Another material deposited with PECVD and used for surface passivation is amorphous silicon (a-Si), which has mainly been applied to heterojunction solar cells in the field of photovoltaics. Annealed in hydrogen, a-Si provides moderate chemical passivation regardless of the substrate doping type. However, AR properties of a-Si are poor opposite to SiN_x, since it absorbs light in the visible wavelength region. [64] Efficient passivation has been demonstrated with a-Si on planar surfaces [65]. On b-Si, however, Montesdeoca-Santan *et. al.* [66] measured only 270 µs carrier lifetime compared to more than 1.5 ms on planar reference sample, indicating significantly more inefficient passivation on the textured surface. The higher SRV was explained

by defects introduced in the c-Si/a-Si interface due to the surface morphology. [66]

In conclusion, although CVD is the predominant deposition method for surface passivation layers in PV industry and impressive results have been demonstrated on planar surfaces, the method cannot provide conformal films onto nanostructured surfaces. Thus, CVD is unsuitable for the passivation of b-Si in general, and focus should be kept on ALD materials.

2.6.5 Stacked ALD SiO_2/Al_2O_3

The formation of negative charge in Al_2O_3 detrimental for n+ surface passivation can be prevented by the deposition of a thin film between the silicon substrate and the Al_2O_3 layer. One of the studied interlayers is SiO_2 [67]. The polarity and amount of charge in SiO_2/Al_2O_3 stacked films was controlled by the SiO_2 interlayer thickness by Dingemans *et. al.* [67] and Terlinden *et. al.* [68]. Charge densities in such stacks deposited by plasma-enhanced atomic layer deposition (PEALD) and PECVD reported by Terlinden *et. al.* are shown in Fig. 7 [68]. Two different regimes in the trend of the charge as a function of the SiO_2 thickness were distinguished. First, the amount of negative charge was observed to decrease rather exponentially as the interlayer thickness was increased. This behaviour refers to electron tunneling: the SiO_2 film acts as a tunneling barrier for electron injection into defect states in Al_2O_3 near the interface. However, direct tunneling is negligible at barrier thicknesses corresponding to the zero-charge condition, i.e. approximately 5 nm for n-type and 11 nm for p-type substrates, in which the charge injection was nearly completely prevented [69]. Therefore, some kind of trap-assisted tunneling mechanism was suggested to be involved in the negative charge formation process. The difference between the curves measured from n- and p-type substrates was explained by different effective tunneling barrier thicknesses caused by different band structures at the Si/SiO_2 interface.

With interlayer thicknesses larger than 13 nm, the total charge in the dielectric stack was dominated by the intrinsic charges in the SiO_2 film. These charges consisted of fixed charges near the Si/SiO_2 interface and bulk charges in SiO_2. The intrinsic charge density was nearly independent of the layer thickness, but depended on the deposition method instead. A moderate charge density (in the range of $4 \cdot 10^{11}$ cm^{-2}) was obtained with PEALD or PECVD, but negligible with thermal oxidation. [68] Similar observations of nearly zero negative charge in oxide stacks with thermal SiO_2 and PECVD Al_2O_3 were made by Mack *et. al.* [70].

In addition to the possibility to control the charge in the passivation layers, significantly low interface defect densities ($<10^{11}$ cm^{-2}eV^{-1}) were measured with SiO_2/Al_2O_3 stacks independent of the interlayer thickness [67]. The high chemical passivation was mainly due to the diffusion of atomic hydrogen from the Al_2O_3 film to the Si/SiO_2 interface during post-deposition annealing [71]. Bare PEALD or PECVD SiO_2, even when annealed in forming gas, was observed to provide insufficient passivation due to high D_{it}. Nevertheless, the deposition of an Al_2O_3 capping film and subsequent annealing reduced the interface defect density substantially and hence increased the effective lifetime with more than one order of magnitude. [72]

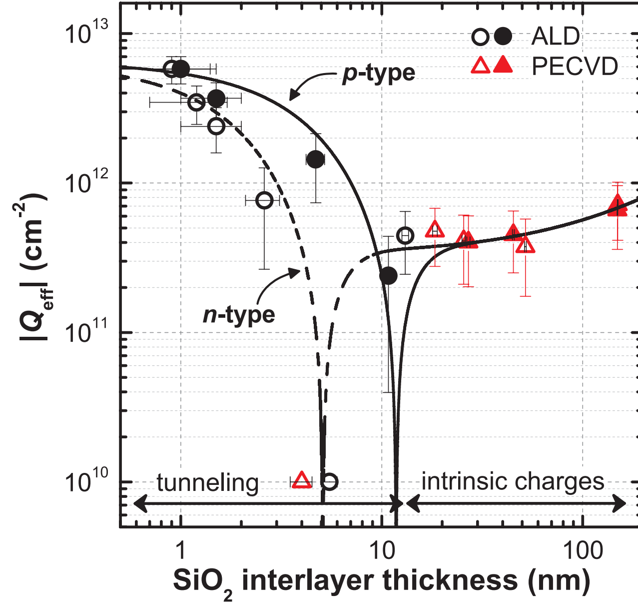

Figure 7: The effective charge density in SiO_2/Al_2O_3 stacked layers deposited by PEALD or PECVD as a function of the SiO_2 interlayer thickness for both n- and p-type substrates. [68]

Also in the case of stacks with thermal SiO_2, Al_2O_3 capped films provided higher lifetimes than those without a capping film. In those stacks, however, the charge density was negligible indicating that the high level of chemical passivation has been the origin of low surface recombination. [73] In addition, wet chemical oxidation or surface pretreatments have been used to enhance the passivation of ALD Al_2O_3 films [74]. These stacks have provided lower interface defect densities compared to H-terminated surfaces. However, the polarity of the fixed charge has been negative. [75]

The passivation properties of SiO_2/Al_2O_3 stacks have been studied also on n+ and p+ emitters. The emitter saturation current density, J_{0e}, was reduced from 81 fA/cm^2 to 50 fA/cm^2 by the deposition of 3.6 nm thick PEALD SiO_2 interlayer between the substrate and an Al_2O_3 film. The reduction of J_{0e} with increasing interlayer thickness on phosphorus emitter was observed to be due to both the improved chemical and field-effect passivation. On p+ surfaces, however, higher J_{0e} values were measured with thicker interlayer films, which is consistent with the fact of reduced amount of negative charge. [76]

Bordihn *et. al.* [77] studied the passivation properties of SiO_2/Al_2O_3 stacks on n+ emitters with a sheet resistance range from 33 Ω/□ to 490 Ω/□. The SiO_2 layers were prepared either by PECVD or a wet chemical oxidation process, in which a thin oxide film was grown in a HCl–H_2O_2 mixture at 85 °C. The positive charge in the PECVD oxide stacks resulted in J_{0e} of 270–12 fA/cm^2 in sheet resistance range of 33–490 Ω/□. Opposite to the polarity of the fixed charge density in the stacks with a PECVD oxide, that of the wet chemically grown oxide stacks was found to be negative by corona charging experiments. As a consequence, such stacks provided

insufficient passivation on phosphorus emitters with sheet resistance larger than $100\,\Omega/\square$. [77] This behaviour is similar to what observed by Hoex *et. al.* in the case of Al_2O_3 thin films, which have a high negative fixed charge density [11]. Thus, it was concluded that surface passivation was highly sensitive to the polarity of the fixed oxide charge in the above-mentioned sheet resistance range. The strength of the field-effect passivation had a smaller effect on emitters with lower sheet resistances as other recombination mechanisms started to limit the lifetime. [77] In conclusion, the positive fixed charge and high interface quality provided by SiO_2/Al_2O_3 stacks are preferable for the surface passivation of n+ emitters. Furthermore, when high conformality characteristic to ALD method is exploited, this passivation scheme should result in effective passivation of b-Si phosphorus emitters.

3 Experimental methods

In order to study surface passivation properly, high quality materials need to be used. If the bulk material is limiting the measured effective lifetime, it is challenging to extract the SRV, which is a merit of the effectiveness of surface passivation (see Section 2.3). Therefore, float-zone (FZ) and magnetic czochralski (CZ) silicon wafers with low impurity levels were used in this study.

For reliable application of the techniques to determine minority carrier lifetime and emitter saturation current density, which will be discussed in Sections 3.2 and 3.3, respectively, it is important that the sample to be characterized is symmetric. Therefore, both sides of the wafers were doped and passivated identically, and b-Si samples had the nanostructure on both surfaces, although the texture would be only on the front surface in a final solar cell. In addition, cleanliness of the process equipment and environment is of remarkable importance, since contamination would kill the lifetime and hence make the study meaningless. Therefore, the cleanliness was ensured by careful monitoring.

In this section, the operating principle of the deposition method utilized in the experimental study of this thesis (Section 4), i.e. atomic layer deposition, is first briefly introduced, followed by discussion on the underlying theory of the applied characterization methods. The latter includes rapid and reliable techniques to characterize the effectiveness of surface passivaton and dielectric film properties, as well as two methods to determine doping profiles in the emitter region.

3.1 Atomic layer deposition

Atomic layer deposition (ALD) is a thin film deposition method widely used in microelectronics industry. Although ALD is currently scarcely used by photovoltaic industry, the application of ALD surface passivation layers for crystalline silicon solar cells is under intensive research in both academia and industrial research units. The technique allows to grow extremely uniform and conformal layers, which is important especially in the case of surfaces with nanoscale features. In addition, ALD ideally enables thickness control with a single atomic layer accuracy. Thus, ALD is usually used when very thin and high-quality layers are required. Furthermore, the ALD films can be deposited at relatively low temperatures, from nearly room temperature to several hundreds of degrees. This is beneficial especially for temperature sensitive materials, such as polymers, and for the contamination control. ALD can be used in the deposition of e.g. oxides and nitrides, which are typical materials used for surface passivation in solar cells. [12]

Currently, the PV industry utilizes a method called chemical vapor deposition (CVD) for the deposition of AR coatings. In CVD, where all process gases are introduced into the reactor simultaneously, the substrate is exposed to only one reactive gas, called precursor, at a time in ALD. Since the different precursors are never present in the reactor simultaneously, the gas molecules can react only with the sample surface, but not with each other in gaseous form. The deposition process proceeds in a self-limiting manner: once all reactive sites on the surface have reacted

with precursor molecules, the growth terminates. After purging the reaction products and the residues of the first precursors from the reactor, the second precursor is introduced and the film growth continues by the next atomic layer. By sequential pulses of the two precursors, a thin film is deposited as shown in Fig. 8. The amount of material deposited on the surface during one growth cycle, i.e. a single exposure to all precursors, is determined by surface–precursor interactions which depend on e.g. the growth temperature. Once the growth per cycle (GPC) characteristic to a process is known, thin film thickness can be determined by the number of cycles. Typical GPC values are around 1 Å/cycle. [12]

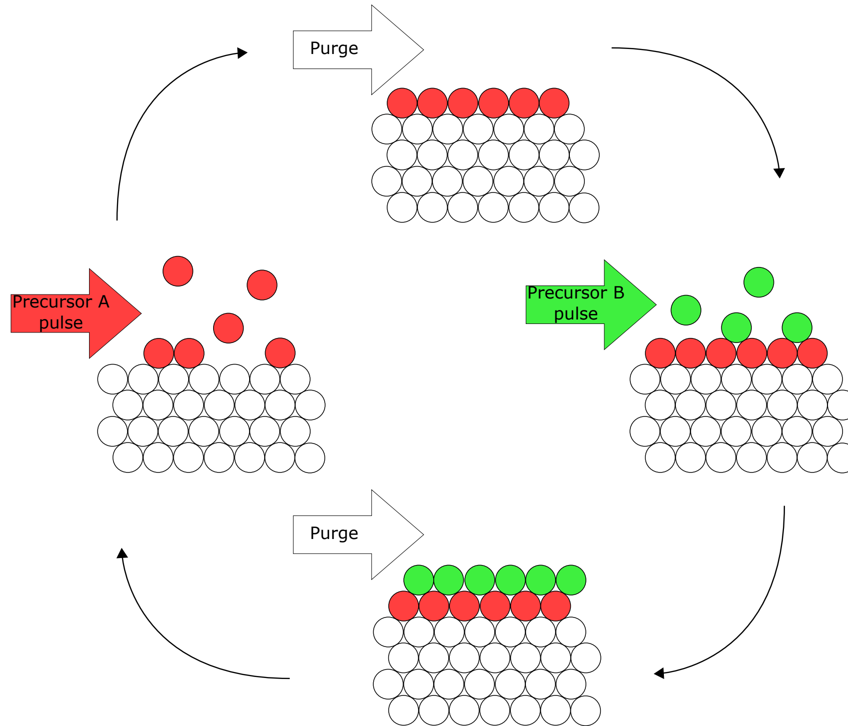

Figure 8: Schematic of an ALD process. Starting from left, precursor A is first conveyed into the reactor. Once all reaction sites have saturated, residues of precursor A and the reaction products are purged from the reactor with an inert gas, e.g. nitrogen (uppermost figure). The process continues by the introduction of precursor B and a subsequent purge. Thin film growth proceeds by sequential pulses of the two precursors.

In practice, several parameters have to be adjusted appropriately in order for ALD process to function as desired. The precursor pulse and subsequent purge steps have to be long enough in order to achieve full adsorption density and to prevent reactions between the gaseous precursors, respectively. The length of one ALD cycle is typically from half to a few seconds. However, deposition on high aspect ratio structures, such as black silicon, may require exceptionally long or several subsequent pulses of the same precursor to ensure that reactive molecules reach the bottom of the trenches [45]. On the other hand, precursor pulses should not be overly long or unwanted side reactions may occur. In addition, sample surface pretreatments affect

the film properties, such as thermal stability, different oxide charges and interface defect density, and hence the passivation quality [74, 75] in solar cell applications.

3.2 Quasi-steady-state and transient photoconductance decay methods

As discussed in Section 2.2, minority carrier lifetime is an important quantity in photovoltaic applications. In addition, cleanliness of processing facilities is usually controlled with regular lifetime measurements from high quality wafers processed with the actual cells. A drop in the lifetime indicates a contamination issue in one or more process equipment. Two non-destructive contactless methods based on the same physical phenomena to measure carrier lifetime are presented here: transient photoconductance decay (PCD) and quasi-steady-state photoconductance (QSSPC) methods.

In the transient PCD method, charge carriers are generated by a rapid light pulse, and decaying conductance of the sample is measured as a function of time after the pulse has terminated. Excess carrier density, Δn, is calculated iteratively from the conductance, σ, and doping and injection dependent carrier mobilities, μ_e and μ_h:

$$\Delta\sigma = q\Delta n(\mu_\mathrm{e} + \mu_\mathrm{h}) \,. \tag{21}$$

Finally, the effective carrier lifetime $\tau_\mathrm{eff,trans}$ as a function of the excess carrier density is obtained from the slope of the measured curve:

$$\tau_\mathrm{eff,trans}(\Delta n) = -\frac{\Delta n(t)}{\mathrm{d}\Delta n(t)/\mathrm{d}t} \,. \tag{22}$$

Transient PCD method is suitable for the measurement of rather long lifetimes only, since considerable excess carrier density has to exist in the sample after the light pulse has finished. The finite turn-off time of the lamp hence limits the valid lifetime range to those larger than approximately 100 µs. [78]

Opposite to the transient PCD method, in the QSSPC technique a sample is subjected to a steady, slowly-decaying pulse of light. The conductance of the sample is measured simultaneously with the light intensity which decays considerably slower than the charge carriers recombine, i.e. the time constant of the lamp is longer than the carrier lifetime. Thus, the carrier densities are in a steady state, and the generation and recombination rates are equal. Under these conditions, the effective minority carrier lifetime can be expressed as a function of the excess carrier density as

$$\tau_\mathrm{eff,QSSPC}(\Delta n) = \frac{\Delta n(t)}{G(t)} \tag{23}$$

where $G(t)$ is the time-dependent generation rate which is calculated from the light intensity. [79]

Compared to the transient PCD method, QSSPC is less prone to noise since it depends on the absolute value of the measured conductance value, rather than on its derivative. In addition, it is capable of measuring very low lifetimes accurately,

since fast measurement electronics, as in transient PCD method, are not required. However, the lifetime is calculated from the absolute value of the generation rate. Therefore, the extracted lifetime value depends on the estimation of the optical constant, i.e. the fraction of the incident light absorbed in the sample. [79] This may be challenging especially in the case of nanostructured surfaces. Moreover, the carrier lifetime has to be considerably shorter than the time constant of the flash in order for Eq. 23 to be valid [79].

The requirement for separate methods for different lifetime ranges can be overcome by a generalized method which combines the two above-mentioned techniques. In general, the effective lifetime can be expressed as

$$\tau_{\mathrm{eff}}(\Delta n) = \frac{\Delta n(t)}{G(t) - \frac{\Delta n(t)}{dt}} \ . \tag{24}$$

In principle, this equation is valid for any minority carrier lifetime or lamp time constant. It can be seen that for conditions $G(t) << \frac{\mathrm{d}\Delta n}{\mathrm{d}t}$ and $G(t) >> \frac{\mathrm{d}\Delta n}{\mathrm{d}t}$, the generalized equation reduces to Eqs. 22 and 23 for transient PCD and QSSPC methods, respectively. In other words, those equations are approximative representations for the relationship between the carrier lifetime and the excess carrier concentration which cause systematic error to the results depending on the actual lifetime in the sample and the lamp time constant. Thus, the generalized model provides more accurate results when the flash intensity decays with a rate comparable to the carrier lifetime. [80]

The two presented methods are simple and rapid techniques to characterize the carrier lifetime in the bulk material or for SRV extraction. Although the methods are not usually applied for the characterization of final solar cells, they give vital information needed for e.g. the development and optimization of different thin film deposition processes utilized for surface passivation purposes. In addition, transient PCD or QSSPC data is used to extract $J_{0\mathrm{e}}$ of emitter samples, which will be discussed next. Thus, these techniques can be utilized also in the emitter design.

3.3 Extraction of emitter saturation current density

As discussed in Section 2.5, the performance of an emitter is usually characterized by emitter saturation current density. The effective lifetime, τ_{eff}, and the emitter saturation current density, $J_{0\mathrm{e}}$, relate to each other according to:

$$\frac{1}{\tau_{\mathrm{eff}}} - \frac{1}{\tau_{\mathrm{Auger}}} = \frac{1}{\tau_{\mathrm{SRH}}} + 2J_{0\mathrm{e}}\frac{(N_{\mathrm{A,D}} + \Delta n)}{qn_{\mathrm{i}}^2 W} \ , \tag{25}$$

where $N_{\mathrm{A,D}}$ is the doping density of the wafer and W is the wafer thickness [81]. The multiplier 2 originates from the assumption of a symmetrical sample which has identical emitters on both sides. Since the emitter recombination term (i.e. the last term on the right-hand side) and the bulk and surface recombination terms have different dependencies on the carrier injection level, $J_{0\mathrm{e}}$ can be determined from the injection level dependence of the lifetime in the high injection level regime. SRH

recombination has a negligible effect on lifetime variation at carrier densities higher than the substrate doping level. [81]

The Auger recombination term, $\tau_{\mathrm{Auger}}^{-1}$, is a known function of carrier density, determined by the commonly accepted Richter model [82]. Thus, the value for the $J_{0\mathrm{e}}$ can be extracted from the slope of the linear region of the measured lifetime curve, when the left-hand side of Eq. 25 is plotted as a function of the injection level, as shown in Fig. 9b. In addition, when the band gap narrowing in the bulk is taken into account, leading to an injection-dependent n_{i}, $J_{0\mathrm{e}}$ can be expressed as: [83, 84]

$$J_{0\mathrm{e}} = \frac{1}{2} qW \frac{\mathrm{d}}{\mathrm{d}\Delta n} \left[n_{\mathrm{i,eff}}^2 \left(\frac{1}{\tau_{\mathrm{eff}}} - \frac{1}{\tau_{\mathrm{Auger}}} \right) \right] , \tag{26}$$

where

$$n_{\mathrm{i,eff}} = n_{\mathrm{i}} e^{\frac{\Delta E_{\mathrm{g}}}{2kT}} \tag{27}$$

is the effective intrinsic carrier concentration where the band gap narrowing, ΔE_{g}, is determined by one of the several existing models [85, 86]. In the Richter model for Auger recombination [82], the band gap narrowing is calculated according to a random-phase approximation model defined by Schenk *et. al.* [86].

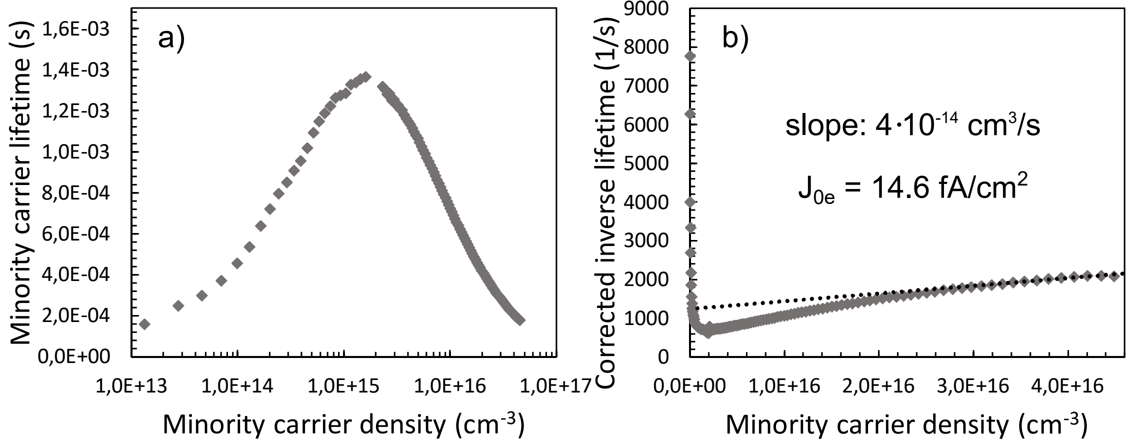

Figure 9: Extraction of $J_{0\mathrm{e}}$ from lifetime data measured with the QSSPC method from a symmetrically diffused emitter sample. a) The original minority carrier lifetime vs. minority carrier density spectrum. b) The left-hand side of Eq. 25 is plotted as a function of carrier density. The inverse lifetime is corrected with the intrinsic bulk lifetime defined by the Richter model [82]. $J_{0\mathrm{e}}$ is calculated from the slope of the linear region at high injection by using Eq. 26 and wafer thickness $W = 490\ \mu\mathrm{m}$. Bending of the curve at high carrier densities could be reduced, and hence the reliability of $J_{0\mathrm{e}}$ extraction enhanced, by using bulk material with lower doping concentration.

3.4 Corona oxide characterization of semiconductor

To be able to develop surface passivation films further, it is essential to understand, which factors have induced the measured minority carrier lifetime or $J_{0\mathrm{e}}$. These

quantities are mainly determined by the properties of the thin film, when the substrate material is of high quality, i.e. the bulk lifetime can be assumed not to be the limiting factor. Therefore, in addition to the lifetime, interface defect density and oxide charge of the thin film are typically determined in order to obtain information about the strength of chemical and field-effect passivation, respectively.

Corona oxide characterization of semiconductor (COCOS) is a non-contact method to study electrical properties, such as dielectric charge and interface defect density, of dielectric films. Electric charge in the form of corona charge, Q_{c}, is deposited on an oxide layer by a high DC voltage applied to a needle electrode close to the sample surface. As a consequence, the electric field in the oxide and in the substrate changes. The response is measured as a contact potential difference in the dark and under strong illumination, $V_{\mathrm{CPD}}^{\mathrm{dark}}$ and $V_{\mathrm{CPD}}^{\mathrm{ill}}$, respectively, with a Kelvin probe. [87] The polarity of corona depends on the polarity of the applied voltage. Under atmospheric conditions, positive corona is predominantly $(\mathrm{H_2O})_{\mathrm{n}}\mathrm{H}^+$ ions [88], whereas negative corona deposits CO_3^- ions [89]. The corona deposition inflicts no damage to the dielectric or the substrate which is a remarkable advantage of the COCOS method [87], although evidence of invasive nature of corona charge has also been demonstrated [90].

An example of a typical V_{CPD} vs. Q_{c} graph measured from an oxide layer deposited on a p-type Si substrate is shown in Fig. 10. The measured contact potential difference consists of a work function difference ϕ_{ms} between the metal electrode and the substrate, a surface barrier V_{sb} and a voltage drop across the oxide layer V_{ox}: [87]

$$V_{\mathrm{CPD}} = \phi_{\mathrm{ms}} + V_{\mathrm{sb}} + V_{\mathrm{ox}} \,. \tag{28}$$

First, negative corona is added on the surface, i.e. the measurement starts from accumulation (left part of Fig. 10). In order to fulfil the electrical neutrality condition, the deposited charge is imaged in the space charge region (ΔQ_{sc}) as well as in interface traps (ΔQ_{it}), i.e. [87]

$$\Delta Q_{\mathrm{c}} = -(\Delta Q_{\mathrm{sc}} + \Delta Q_{\mathrm{it}}) \,, \tag{29}$$

as shown in Fig. 11a in the context of an energy band diagram corresponding the accumulation condition. The charge in the depletion region, Q_{sc}, can be determined from a theoretical model and depends on the surface barrier, V_{sb}, at the silicon–oxide interface. Subsequently, positive corona charge, ΔQ_{c}, is added in small doses, which changes the voltage drop across the oxide layer and the surface barrier, whereas ϕ_{ms} remains constant. Thus, [87]

$$\Delta V_{\mathrm{CPD}} = \Delta V_{\mathrm{ox}} + \Delta V_{\mathrm{sb}} \,. \tag{30}$$

An interesting point in the (Q_{c},V_{CPD}) curve is the charge value, in which the $V_{\mathrm{CPD}}^{\mathrm{dark}}$ and $V_{\mathrm{CPD}}^{\mathrm{ill}}$ curves diverge, since it defines the flat band voltage, V_{FB}. An energy band diagram corresponding the flat band condition is shown in Fig. 11b, from which it can be seen that $V_{\mathrm{sb}} = 0$. This point is employed in the determination of an important parameter, the total charge Q_{tot}. It is defined as the Q_{c} difference

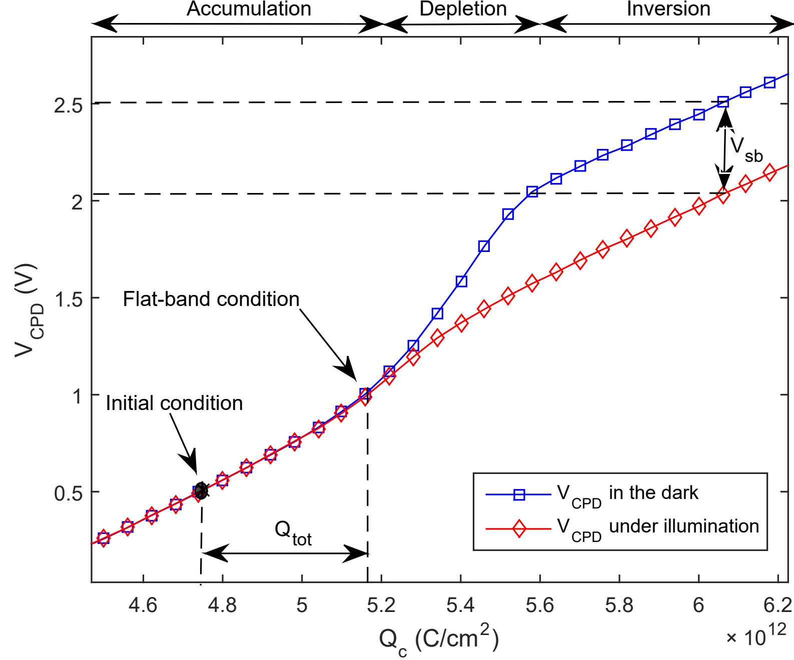

Figure 10: Contact potential difference as a function of added corona charge measured from a SiO_2/Al_2O_3 dielectric stack on p-type Si. Total charge in the oxide (Q_{tot}) is equal to the charge difference between the points corresponding initial and flat band conditions. According to Eq. 35, surface band bending is the difference in V_{CPD} measured in the dark and under high illumination. Interface defect density (D_{it}) is determined from the range between the flat band and high inversion conditions, i.e. from the depletion regime. The slight non-linearity in the V_{CPD} measured under illumination (red curve) is due to insufficient LED power of the measurement equipment to collapse the surface barrier under inversion.

between the points corresponding the initial and flat band conditions, as depicted in Fig. 10. In order to fulfil the electrical neutrality condition, the total charge obeys the following relationship: [87]

$$Q_{\mathrm{tot}} = Q_{\mathrm{ox}} + Q_{\mathrm{it}}^{\mathrm{FB}} + Q_{\mathrm{surf}}\ , \tag{31}$$

where Q_{ox} is the oxide charge, $Q_{\mathrm{it}}^{\mathrm{FB}}$ is the interface trapped charge under the flat band condition and Q_{surf} is any initial charge on the dielectric surface. Thus, the total charge is an effective parameter to study the formation of any kind of charge into or onto an oxide. In Eq. 31, the oxide charge denotes the sum of different types of charges in the oxide layer, including fixed charge Q_{f}, oxide trapped charge Q_{ot} and mobile charge Q_{m} (recall Section 2.3.1):

$$Q_{\mathrm{ox}} = Q_{\mathrm{f}} + Q_{\mathrm{ot}} + Q_{\mathrm{m}}\ . \tag{32}$$

Only the latter one changes as a function of Q_{c}. [87]

After the flat band condition, depletion and finally inversion (Fig. 11c) are achieved by incremental positive corona addition. $V_{\mathrm{CPD}}^{\mathrm{dark}}$ and $V_{\mathrm{CPD}}^{\mathrm{ill}}$ diverge, since

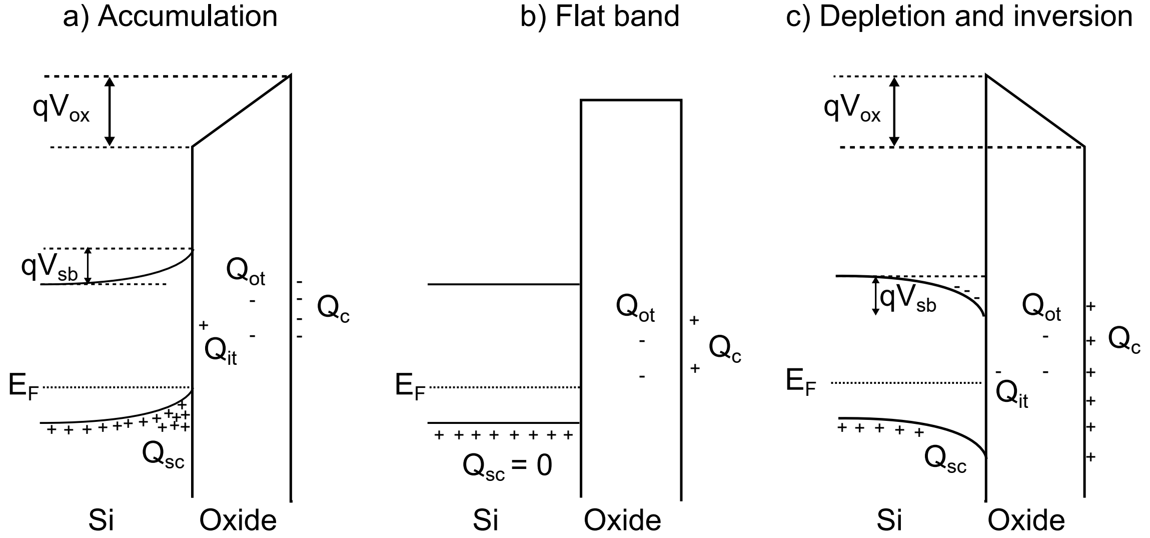

Figure 11: Effect of corona charge on the band structure of p-type silicon–dielectric structure. a) Accumulation induced by negative oxide trapped (Q_{ot}) and corona charges (Q_c). Deposited charge is imaged in the space charge region (Q_{sc}) and in interface traps (Q_{it}). b) Flat band condition. The addition of positive corona charge changes the amount of Q_{it} and Q_{sc}, but the oxide-trapped charge remains constant. c) Incremental positive corona addition induces first depletion and finally inversion. In addition, surface barrier (V_{sb}) and potential difference over the oxide (V_{ox}) are indicated.

strong illumination flattens the surface barrier in depletion. Thus, according to Eq. 30, $V_{\mathrm{CPD}}^{\mathrm{dark}}$ and $V_{\mathrm{CPD}}^{\mathrm{ill}}$ can be expressed as

$$\Delta V_{\mathrm{CPD}}^{\mathrm{dark}} = \Delta V_{\mathrm{ox}} + \Delta V_{\mathrm{sb}} \quad \text{and} \tag{33}$$

$$\Delta V_{\mathrm{CPD}}^{\mathrm{ill}} = \Delta V_{\mathrm{ox}} \,. \tag{34}$$

Based on Eqs. 33 and 34, the surface barrier can be determined as the difference between the contact potential differences measured in the dark and under illumination: [87]

$$\Delta V_{\mathrm{CPD}}^{\mathrm{dark}} - \Delta V_{\mathrm{CPD}}^{\mathrm{ill}} = \Delta V_{\mathrm{sb}} \,. \tag{35}$$

The region corresponding the depletion condition is important also in the sense that the interface trap density D_{it} is determined based on those values. From Eq. 29 based on the charge neutrality requirement, charge added to interface traps is equal to the difference between the added corona charge and the corresponding change of the depletion region charge: [91]

$$|\Delta Q_{\mathrm{it}}| = |\Delta Q_{\mathrm{c}}| - |\Delta Q_{\mathrm{sc}}| \,. \tag{36}$$

Values for Q_{it} can be calculated from the above equation, since ΔQ_{c} is a known amount of deposited charge and ΔQ_{sc} is determined from a theoretical model based on V_{sb} which is calculated from Eq. 35. The interface trap density is finally obtained

from a relation [91]

$$D_{\mathrm{it}} = \frac{\Delta Q_{\mathrm{it}}}{\Delta V_{\mathrm{sb}}} \quad \text{or in a differential form} \quad D_{\mathrm{it}} = \frac{dQ_{\mathrm{it}}}{dV_{\mathrm{sb}}} \,. \tag{37}$$

To characterize the interface traps in more detail, D_{it} is usually plotted as a function of V_{sb}. This so-called D_{it} spectrum interprets the energy distribution of the traps across the energy band gap. If only a single value is reported, minimum or mid-gap value is usually used. Examples of D_{it} spectra can be found from Figs. 13b and 15b in the context of the experimental results.

3.5 Charge density from contact potential difference

Some dielectric films, e.g. thermal SiO_2 [48], contain only a small amount of fixed charge, and hence the surface passivation is almost entirely achieved by low D_{it} provided by the film. In order to enhance field-effect passivation, or to study the effect of field-effect passivation strength variation on lifetime or $J_{0\mathrm{e}}$, corona charge is often deposited onto the dielectric film. For quantitative characterization of the relation between the amount of deposited charge and e.g. $J_{0\mathrm{e}}$, the exact charge density which is deposited has to be determined.

As stated by Eq. 34, the change in the contact potential difference measured under illumination equals the change in the voltage drop over the oxide layer. This property can be utilized to determine an increase or decrease in the surface charge density when the change in the amount of other charges is considered to be negligible. Thus, the amount of corona charge, ΔQ_{c}, deposited onto a sample to modify the electric field at the surface can be verified.

A system consisting of a Kelvin probe, a dielectric film and a substrate, i.e. similar structure as discussed in the previous section, can be considered as a plate capacitor. The capacitance C of such structure is given by

$$C = \epsilon_{\mathrm{r}}\epsilon_0 \frac{A}{t_{\mathrm{ox}}} \,, \tag{38}$$

where ϵ_0 is the dielectric constant, A is the area of the capacitor and ϵ_{r} and t_{ox} are the relative permittivity and the thickness of the dielectric layer, respectively. On the other hand, capacitance is defined as the ratio of charge and voltage difference, ΔQ and ΔV, respectively:

$$C = \frac{\Delta Q}{\Delta V} \,. \tag{39}$$

Thus, a change in the areal charge density ($\mathrm{C/cm^2}$) can be determined from a change in the potential difference when the dielectric constant and oxide thickness are known:

$$\frac{\Delta Q_{\mathrm{c}}}{A} = \epsilon_{\mathrm{r}}\epsilon_0 \frac{\Delta V_{\mathrm{ox}}}{t_{\mathrm{ox}}} \,. \tag{40}$$

Eq. 40 can be extended for stacks of two or more dielectric films with different properties, when the layers are considered as separate capacitors in series. The total

capacitance of a stack of two dielectric films with thicknesses t_1 an t_2 and dielectric constants $\epsilon_{\mathrm{r},1}$ and $\epsilon_{\mathrm{r},2}$ is

$$C_{\mathrm{tot}} = \frac{C_1 C_2}{C_1 + C_2} = \epsilon_0 A \frac{\epsilon_{\mathrm{r},1}\epsilon_{\mathrm{r},2}}{\epsilon_{\mathrm{r},1} t_2 + \epsilon_{\mathrm{r},2} t_1} \,. \tag{41}$$

The deposited areal charge density can then be calculated from the following equation:

$$\frac{\Delta Q_{\mathrm{c}}}{A} = \frac{C_{\mathrm{tot}}}{A}\Delta V_{\mathrm{ox}} = \epsilon_0 \frac{\epsilon_{\mathrm{r},1}\epsilon_{\mathrm{r},2}}{\epsilon_{\mathrm{r},1} t_2 + \epsilon_{\mathrm{r},2} t_1}\Delta V_{\mathrm{ox}} \tag{42}$$

In order for this approximation to be valid, the films should be rather uniform, which usually is the case with ALD thin films. For the above equation, the film thicknesses and ΔV_{ox} can be determined e.g. with an ellipsometer and a Kelvin probe, respectively. The relative permittivities can either be taken as table values or determined by traditional C–V or COCOS measurements.

3.6 Characterization of emitter doping profiles

To be able to study emitter formation and the effect of different diffusion process parameters on the resulting emitter, it is important to know the diffused dopant concentration as a function of depth in a sample. In addition, diffusion profiles give valuable information regarding the electric properties of the heavily doped region of a solar cell, as discussed in Section 2.5.

One technique to determine doping profiles in silicon is called electrochemical capacitance–voltage (ECV) profiling. In this method, capacitance of an electrolyte–semiconductor Schottky contact is measured at a constant DC bias voltage. The depth profile can be measured as silicon is electrolytically etched between sequential capacitance–voltage measurements. No depth limits are set by the technique. However, it is destructive since material is etched away from the sample as the measurement proceeds and capable of measuring the concentration of electrically active dopants only. [15]

In some occasions, total concentration of dopants gives important information about the properties of an emitter. This total doping concentration, including possible non-activated dopants as in the case of a dead layer, can be measured e.g. with secondary ion mass spectroscopy (SIMS). In this technique, material is removed from a sample by physical sputtering, and the secondary ions are detected and analysed by an energy filter and a mass spectrometer as a function of time. After the measurement, the depth of the resulting crater is determined with e.g. profilometer, thus enabling the conversion from sputtering time to depth in the sample, assuming a constant sputtering rate. This assumption requires the sample to be rather homogeneous within the depth of the crater. Finally, the secondary ion signal is converted to dopant concentration by utilizing a calibration data from a reference sample. For instance, phosphorus is implanted into a wafer with a known energy and dose, and the secondary ion signal from this reference is calibrated by assuming the total amount of phosphorus ions to equal the amount of implanted phosphorus.

The intensity of the measured signal from an unknown profile is then compared to this reference. [15]

According to present knowledge, neither of these two techniques are able to determine the doping profiles in b-Si. In the case of ECV, the etch rate of a nanostructured surface is not precisely defined, which results in remarkable inaccuracy in depth. In SIMS instead, the primary ion beam and the crater area are considerably larger compared to the features of the nanostructure. Therefore, the technique cannot distinguish between separate silicon needles or an ion sputtered from the top of a spike from that ejected from the bottom of a groove. Due to these challenges, doping profiles are determined only from planar samples in this study, and the characterization of doping concentration in b-Si is limited to sheet resistance measurements.

4 Results and discussion

The goal of the experiments presented in this section was to first reproduce deposition processes for thin films with positive fixed charge introduced in Section 2.6, and then to demonstrate their passivation quality on b-Si phosphorus emitters. The study was begun with thermal oxide, as oxidation processes are well known in general and they grow conformally even on nanoscale structures [12], which is important for the surface passivation of b-Si.

4.1 Hydrogen annealed SiO_2

First trial to achieve a high density of positive fixed charge in a thin film was performed by annealing thermal oxide in hydrogen ambient, based on the literature discussed in Section 2.6.3. Substrate material was p-type FZ silicon with <100> orientation, thickness of 250 μm and resistivity of 1 Ωcm. The wafers underwent the standard SC1+SC2+HF cleaning sequence and were oxidized in O_2 ambient in Centrotherm furnace at 900 °C for 40 minutes with target thickness of 15 nm. The exact oxide thickness was measured with PLASMOS SM 2300 ellipsometer. Subsequently, one wafer was annealed in pure hydrogen at 600 °C for 30 minutes in Jipelec JetFirst rapid thermal processor. The furnace was first evacuated and subsequently filled with hydrogen to reach a 99 Torr pressure corresponding 0.13 atm, which was the maximum pressure allowed for H_2 processes in the tool in question. Temperature was ramped up to the annealing temperature in H_2 ambient, but cooled back to room temperature in nitrogen after the annealing. Effective minority carrier lifetime was determined with Sinton Instruments WCT-120 lifetime tester utilizing the generalized method described in Section 3.2. Finally, COCOS measurements were performed with Semilab PV-2000 lifetime scanner in order to investigate the oxide charge and interface defect density, as discussed in more detail in Section 3.4.

A total charge density in the order of $1 \cdot 10^{10}$ cm^{-2} was measured from the hydrogen annealed sample with thermal silicon dioxide. Although the D_{it} was below 10^{11} cm^{-2}eV^{-1}, the negligible charge density resulted in a low lifetime of only 64 μs. Thus, this study failed to replicate the high positive charge density reported by Vanheusden *et. al.* [55] and Afanas'ev *et. al.* [56]. The annealing conditions, however, differed from the reported ones due to instrumental limitations. In the literature discussed in Section 2.6.3, the H_2 annealing was performed in 1.1 atm pressure and the samples were cooled in an unaltered ambient. However, such conditions were infeasible with the tools at Micronova Nanofabrication Centre, and a lower pressure of 0.13 atm was applied instead. In addition, the annealing furnace was purged of hydrogen with nitrogen before cooling due to the tool limitations. As a consequence, the hydrogen annealed sample experienced a subsequent high temperature treatment in N_2 ambient during the temperature ramp-down. This may have dissociated the hydrogen atoms from strained Si–Si bonds and hence removed the positive charge possibly formed during the H_2 annealing, similar to what has been reported to occur with a vacuum annealing [55, 56].

4.2 Thermal vs. ALD SiO_2 interlayer for stacked films

Since the hydrogen annealing experiments were unsuccessful, the study was continued with another promising n+ emitter passivation scheme arisen from the literature review. Before experiments with actual emitter samples, the study of the stacked layers was begun with uniformly doped planar wafers in order to investigate how well the results reported in literature and discussed in Section 2.6.5 can be replicated. First, the passivation quality of SiO_2/Al_2O_3 stacks with either thermal or PEALD SiO_2 are compared.

Same substrate material as above was used for the experiments. Two wafers were oxidized with the above-mentioned parameters with target thickness of 15 nm. One of these wafers experienced a subsequent 20 minutes annealing in nitrogen ambient at the same temperature, while the other was directly cooled back to room temperature after the oxidation. The exact oxide thickness was confirmed with ellipsometer and effective minority carrier lifetime was measured with the lifetime tester. After the measurement, the wafers were cut in half. 22 nm of Al_2O_3 was deposited on both sides of one of the halves by thermal TMA + H_2O ALD process at 200 °C in Beneq TFS-500 tool. Similar oxide thickness and lifetime measurements were conducted after the deposition. Post-deposition annealing was performed at 400 °C for 30 min in nitrogen ambient in PEO furnace to enhance the surface passivation provided by the oxide stack. Finally, lifetime, interface defect density and charge density were measured with QSSPC and COCOS methods, respectively.

Another set of SiO_2/Al_2O_3 stacks was fabricated in a continuous ALD process sequence. 15 or 30 nm of SiO_2 was first deposited on one side of HF-treated samples by PEALD with AP-LTO 330 and O_2 plasma as the silicon and oxygen precursors, respectively. This was followed by a thermal Al_2O_3 ALD process (TMA and H_2O as precursors) targeting for a 30 nm thickness in the same reactor without pressurizing the chamber in between. Both depositions were performed at 200 °C. The samples were turned over, and the other sides were processed similarly. After the deposition, the resulted thicknesses were confirmed with ellipsometer, and the post-deposition annealing and measurements were performed as in the case of the thermally oxidized samples.

Minority carrier lifetimes of the samples passivated by SiO_2/Al_2O_3 stacks with either thermal or PEALD SiO_2 measured at an injection level of $1 \cdot 10^{15}$ cm^{-3} are presented in Fig. 12. Values are given for both as-deposited and annealed states for all samples. In addition, lifetimes of the thermally oxidized wafers prior to the Al_2O_3 deposition are shown.

Bare thermal silicon dioxide passivates the sample surfaces insufficiently. This can be explained by a low, less than $2{\cdot}10^{11}$ cm^{-2} total charge density in the oxide as shown in Fig. 13. In addition, the polarity of the charge is not optimal for p-type substrates. Electric field induced by the positive fixed charges attracts minority carriers, i.e. electrons, to the surface and hence bends the energy bands towards the flat band condition. Moreover, the charge density is too low to achieve inversion. Although the interface quality between silicon and SiO_2 is high, the deficiency of field-effect passivation results in a low lifetime.

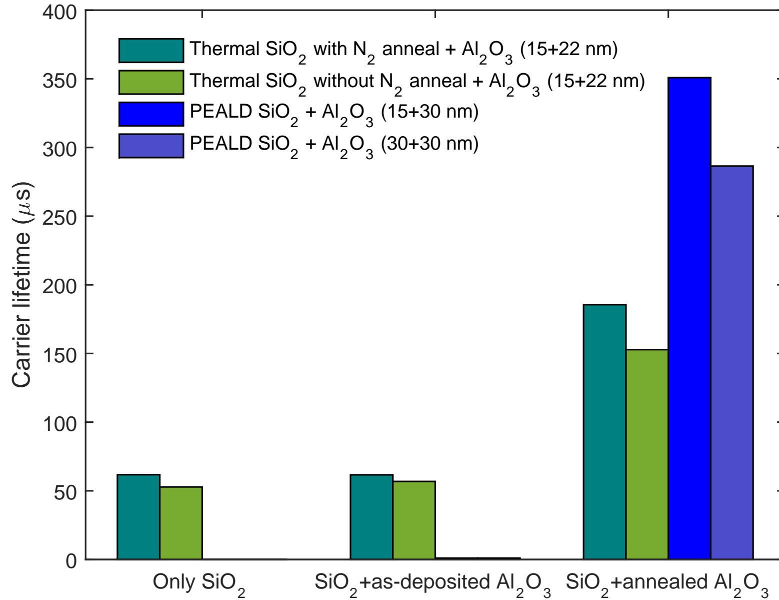

Figure 12: Minority carrier lifetime measured from planar samples passivated with SiO_2/Al_2O_3 stacks with either thermal or PEALD SiO_2 at an injection level of $1 \cdot 10^{15}$ cm^{-3}. Values are given for both as-deposited and annealed states. For the thermal oxide samples, lifetimes prior to Al_2O_3 deposition are also presented.

The deposited Al_2O_3 has only a minor effect on the lifetime in the as-deposited state. Nevertheless, annealing improves the lifetime approximately by a factor of three. This in in accordance with literature, as ALD Al_2O_3 films have usually been reported to require a post-deposition annealing to provide sufficient passivation [36,65]. The increased lifetime can be ascribed to enhanced chemical passivation and a change in the total charge polarity. The mid-gap D_{it} is reduced from $1.5 \cdot 10^{11}$ to $7.6 \cdot 10^{10}$ $cm^{-2}eV^{-1}$ and from $2.6 \cdot 10^{11}$ to $1.3 \cdot 10^{11}$ $cm^{-2}eV^{-1}$ for the samples with and without nitrogen-annealed oxide layers, respectively. This improvement of the interface quality is consistent with the literature discussed in Section 2.6.5 and can be attributed to the diffusion of atomic hydrogen from the Al_2O_3 capping layer to the Si–SiO_2 interface states during the annealing process [71]. The sample with nitrogen-annealed oxide shows slightly higher lifetime than the other thermally oxidized sample, which can be explained by the lower interface defect density. However, 15 nm of thermal SiO_2 is unable to completely prevent negative charge formation in the Al_2O_3 film, and the net charge of the stacks changes from slightly positive into negative which is not preferential for phosphorus emitter passivation.

The as-deposited ALD SiO_2/Al_2O_3 stacks provide negligible surface passivation, as can be seen from the middle column of Fig. 12. The measured lifetime values are only several microseconds which is already in the lower limit of the measurement range. Annealing was required to activate the passivation. The increased carrier lifetime can be attributed to both enhanced chemical and field-effect passivation.

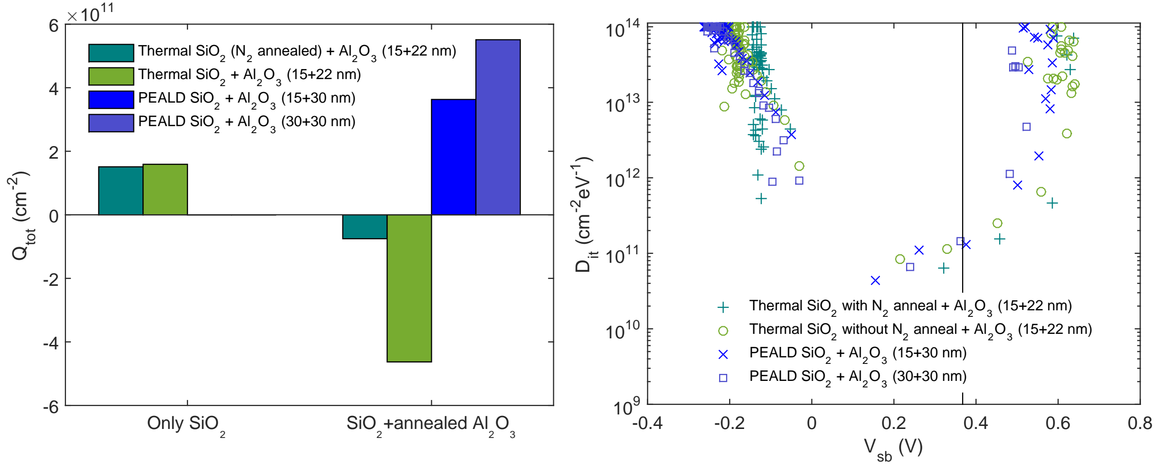

Figure 13: Total charge (Q_{tot}) and interface defect density (D_{it}) spectra measured from planar samples passivated with SiO_2/Al_2O_3 stacks with either thermal or PEALD SiO_2. For the thermal oxide samples, values measured prior to Al_2O_3 deposition are also presented. The solid line represents the mid-gap position in the D_{it} plot.

Positive fixed charge densities were measured from the ALD SiO_2/Al_2O_3 bilayers which is in accordance with the literature discussed in Section 2.6.5. The interface defect densities of the annealed ALD stacks are comparable to those of stacks with thermal oxide as can be noticed from the D_{it} spectra in Fig. 13. The mid-gap values are in the range of $1 \cdot 10^{11}$–$2 \cdot 10^{11}$ cm^{-2}eV^{-1} which are comparable to or even lower than those usually measured from surfaces passivated with ALD Al_2O_3 [36].

The ALD stack with 15 nm of SiO_2 is observed to contain less charge compared to the 30 nm interlayer stack. The lower areal charge density can be attributed to a smaller volume and thus to a lower amount of bulk and oxide trapped charge in the SiO_2 thin film. In addition, the ALD stack with a 15 nm interlayer provides slightly more efficient surface passivation. This is in connection with lower density of positive charge and the slightly lower interface defect density, $2.4 \cdot 10^{11}$ cm^{-2}eV^{-1} compared to $1.7 \cdot 10^{11}$ cm^{-2}eV^{-1}. Since positive charge is unfavourable for the field-effect passivation of p-type surfaces and the substrate material is rather heavily doped (1 Ωcm resistivity), a higher density of positive charge in the 30 nm interlayer stack brings the surface closer to flat band condition but not until inversion and thus towards a higher recombination rate. In addition, the shorter distance between the silicon substrate and the capping layer with a thinner interlayer may have induced more efficient atomic hydrogen diffusion into the interface defects and hence be the origin of the lower D_{it}.

4.3 Film and passivation properties of ALD SiO_2/Al_2O_3

Since the SiO_2/Al_2O_3 stacks with thermal oxide provided fixed charge of unsuitable polarity, the study was continued with the ALD stacks. However, the lifetime values shown in Fig. 12 were comparatively low also for the ALD version. This is

partly due to the fact that the existing processes used in the first tests were created without considering any surface passivation aspects. Therefore, several ALD process development runs were performed to optimize the parameters for the deposition of each layer, i.e. SiO_2 and Al_2O_3. As the deposition temperature was fixed to 200 °C in the literature [67, 68], precursor pulse and purge lengths were chosen as the parameters to be varied.

For the ALD process development for black silicon, two different p-type silicon substrate materials were used: in addition to the wafers used for the first trials mentioned above, FZ-Si samples with <100> orientation, 400 μm thickness and 3 Ωcm nominal resistivity were used. b-Si was first etched on both sides of HF-treated wafers with cryogenic DRIE using Oxford Instruments Plasmalab System 100 at -120 °C. SF_6/O_2 plasma process with inductively and capacitively coupled plasma powers set to 1000 W and 2 W, respectively, was used for 7 minutes in 10 mTorr pressure. The SF_6 and O_2 gas flow rates were 40 and 18 sccm, respectively. One b-Si and one planar reference sample were processed simultaneously in all process steps from this point onward. After the etching, the samples were SC1 cleaned and dipped in 1 % HF solution, followed by the deposition of SiO_2/Al_2O_3 stacks in a similar manner as described above for the planar wafers. Film thicknesses of 15 and 30 nm for SiO_2 and Al_2O_3, respectively, were targeted in all runs and confirmed with ellipsometer. Subsequent annealing and measurement steps were performed as described earlier. Based on the obtained results, different ALD precursor pulse lengths and sequences were applied for several sample pairs (planar and b-Si) according to Table 1.

Table 1: Precursor pulse lengths and subsequent purge times for PEALD SiO_2 and thermal ALD Al_2O_3 processes applied in different runs. AP-LTO 330 and O_2 plasma were the Si and O precursors for SiO_2, and TMA and H_2O were the Al and O precursors for Al_2O_3. N_2 was used for purging.

Run	**Description**	**AP-LTO 330 + purge**	**O_2 plasma + purge**	**TMA + purge**	**H_2O + purge**
#1	single pulse	200 ms 500 ms	2 s 2 s	200 ms 2 s	300 ms 4 s
#2	double pulse	200+200 ms 500 ms	2 s 2 s	200+200 ms 2 s	250+250 ms 4 s
#3	double pulse (longer)	500+500 ms 500 ms	5 s 2 s	200+200 ms 2 s	250+250 ms 4 s
#4	double pulse (SC2)	300+300 ms 500 ms	3 s 3 s	200+200 ms 2 s	250+250 ms 4 s

The efficiency of surface passivation between different runs is compared as surface recombination velocity instead of carrier lifetime in Fig. 14. Thus, the passivation quality of thin films on wafers with different thicknesses can be compared more

directly. In addition, the effect of bulk lifetime has been taken into account by using Eq. 15 in order to improve the comparability of the values measured from substrates with different doping concentrations. According to the model presented in [92], p-type wafers with a resistivity of 1 Ωcm and 3 Ωcm have a bulk lifetime of 1.95 ms and 8.08 ms, respectively.

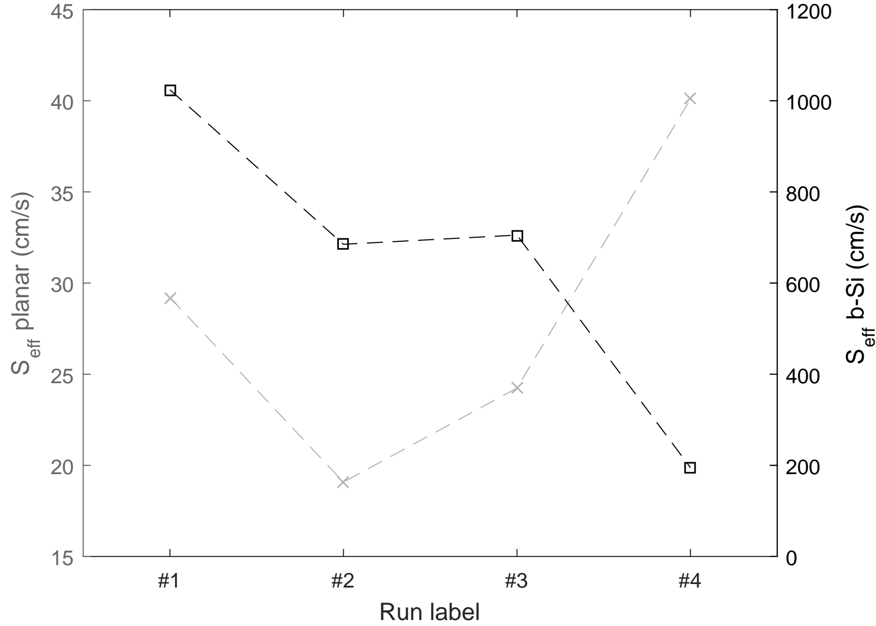

Figure 14: Surface recombination velocities (S_{eff}) measured from planar (grey) and b-Si (black) samples passivated with SiO_2/Al_2O_3 stacks deposited by ALD. Note the separate axes for planar and b-Si. Parameters corresponding the labels are presented in Table 1.

The first stacks were deposited by applying already existing recipes for both SiO_2 and Al_2O_3 with single pulses of all precursors, i.e. AP-LTO 330 and O_2 plasma for SiO_2 and TMA and water for Al_2O_3 (see the first row in Table 1). This process was applied also for samples presented in Section 4.2. As can be seen from Fig. 14, the single pulse scheme resulted in extremely high SRV in the b-Si sample. Insufficient passivation was most probably caused by too short precursor pulses. Since b-Si structure consists of sharp silicon needles and deep valleys in between, rather long ALD precursor pulses are usually required in order to achieve conformal deposition. With shorter pulse lengths the precursor gas molecules have insufficient time to reach the bottom of the valleys.

As a consequence, longer precursor pulses were applied in the second run (#2 in Table 1). The pulse lengths of AP-LTO 330 and TMA were doubled and that of H_2O increased by 200 ms, whereas the O_2 plasma and purge steps were kept constant. The plasma pulse time was not changed due to its different nature compared to the other pulses. In the used ALD tools, the precursor gases were fed by their line pressures. In order to ensure that the pressures remain at sufficient level and hence

the gas flows rather constant while the valves to the reactor are open, the lengthened pulses were divided into two equally long sequential parts. Example was taken from another ALD tool, where similar pulsing scheme has provided excellent film quality. This double pulse process resulted in lower SRV in both planar and b-Si samples (Fig. 14). In planar sample, a SRV of less than 20 cm/s was achieved corresponding to near millisecond lifetime. In b-Si, however, the value was still high, and even longer pulses were applied in the third run (#3). Also the O_2 plasma exposure time was increased this time. Significant undergrowth, i.e. film growth on the side which was against the plate, was observed on the processed samples. In addition, the GPC was slightly higher compared to the previous runs. Thus, the lengthening of the precursor pulses while keeping the purge steps constant resulted in CVD growth, which made the passivation quality even worse (#3 in Fig. 14).

Q_{tot} and D_{it} of the annealed films determined by COCOS method are presented in Fig. 15. D_{it} is reported only for the planar samples since its extraction from COCOS measurements in the case of b-Si is not yet unambiguously defined. The charge is positive in films deposited in the first three runs with different process parameters as expected based on the literature review (Section 2.6.5). Approximately 4–7 times higher charge density was measured from b-Si samples compared to the planar references, which is in agreement with the previously reported results [8] (recall Fig. 6). The D_{it} spectra of the samples from runs #1 and #2 have no significance difference and show good interface quality with less than $2 \cdot 10^{11}\ \mathrm{cm}^{-2}\mathrm{eV}^{-1}$ mid-gap D_{it}. However, the thin film deposited in run #3 shows considerably poorer interface quality, especially when the lowest point is excluded from the inspection as a single outlier. This observation is in accordance with the observed CVD growth and higher SRV.

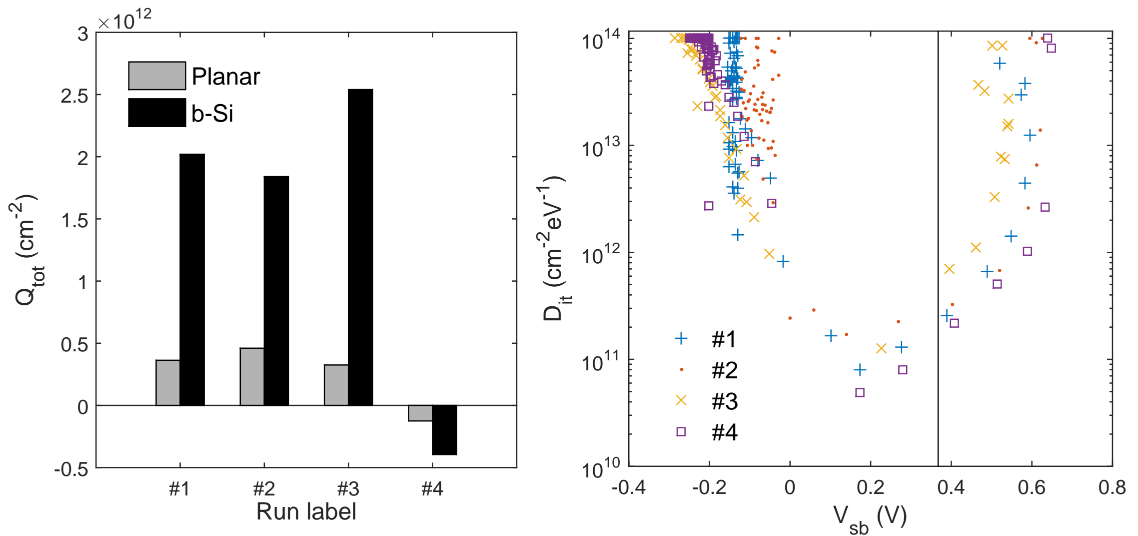

Figure 15: Total charge (Q_{tot}) and interface defect density (D_{it}) spectra measured from samples passivated with SiO_2/Al_2O_3 stacks deposited by ALD. The solid line represents the mid-gap position in the D_{it} plot. Parameters corresponding the labels are presented in Table 1.

Since diluted SC2 pretreatment has shown to improve the passivation quality in the case of ALD Al_2O_3 significantly [74], one sample pair underwent an additional SC1 + diluted SC2 cleaning sequence prior to the thin film deposition. The amounts of HCl and H_2O_2 were diluted by factors 40 and 10, respectively. Contrary to the hypothesis of improved surface passivation, the SRV of the planar sample increased significantly compared to the other processes. In addition, COCOS measurements revealed the oxide charge to be negative instead of positive. Negative charge has been observed in SiO_2/Al_2O_3 stacks in earlier studies, in which the SiO_2 had been wet-chemically grown [75]. However, those stacks had no PEALD SiO_2 layer. The suppression of positive charge formation by the thin chemical oxide layer implies that the positive charge in the stacks has interfacial characteristics. Nevertheless, the lowest D_{it} is obtained with the diluted SC2 pretreated sample, which is in accordance with literature [74, 75].

Opposite to the planar sample, the diluted SC2 treated b-Si sample shows the best passivation quality among the b-Si samples (run label #4 in Fig. 14). This could partly be explained by the charge sensitivity of surface passivation of b-Si. As the lifetime in b-Si is effected more radically on the charge in the passivation layer [8] as discussed in Section 2.4.3, the charge polarity change from positive to negative affects the SRV more significantly than in the planar case. The positive charge density formed in the runs #1–#3 may be insufficient to achieve inversion in p-type b-Si and result in condition close to flat-band, hence providing poor passivation. On planar surfaces instead, inversion can be achieved with a lower oxide charge density. Thus, inversion in the case of runs #1–#3 may be stronger than accumulation in the run #4 sample due to a lower absolute value of charge density, which may be the reason of weaker passivation.

Another explanation could be a larger improvement in the interface quality. If the stacks formed rather poor interface with b-Si, the wet chemical oxide would improve the D_{it} considerably. In the planar case, equally large difference may not be visible in lifetime as the interface quality was already sufficient. Despite the improvement, the SRV is still comparatively high in b-Si, since the charge density is low (approximately $-4{\cdot}10^{11}\,\mathrm{cm}^{-2}$ on b-Si). Although the diluted SC2 pretreatment resulted in the lowest SRV in p-type b-Si, it would impair the passivation of n+ emitters due to the unfavourable charge polarity. Therefore, HF-dip is concluded to be a more favourable pretreatment prior to the deposition of the stacks for that application. The use of n-type Si wafers for these experiments would have afforded more grounds for this discussion, as the type of the surface had been the same with the phosphorus emitters.

Finally, the b-Si structure and conformality of the deposited ALD SiO_2/Al_2O_3 bilayer coating on a nanostructured surface was inspected by taking scanning electron microscope (SEM) images with Zeiss Supra 35 tool from a b-Si sample covered with the thin films. The double pulse process (#2) was applied for the deposition on the studied sample. An SEM image of 15 nm of SiO_2 and 30 nm of Al_2O_3 on b-Si is shown in Fig. 16. The white areas arise from the dielectric film which can be noticed to follow the underlying nanostructures extremely well. From the inset with a smaller scale, even the two different films can be distinguished. Based on

the image, the films can be concluded to be rather conformal which is essential for efficient surface passivation.

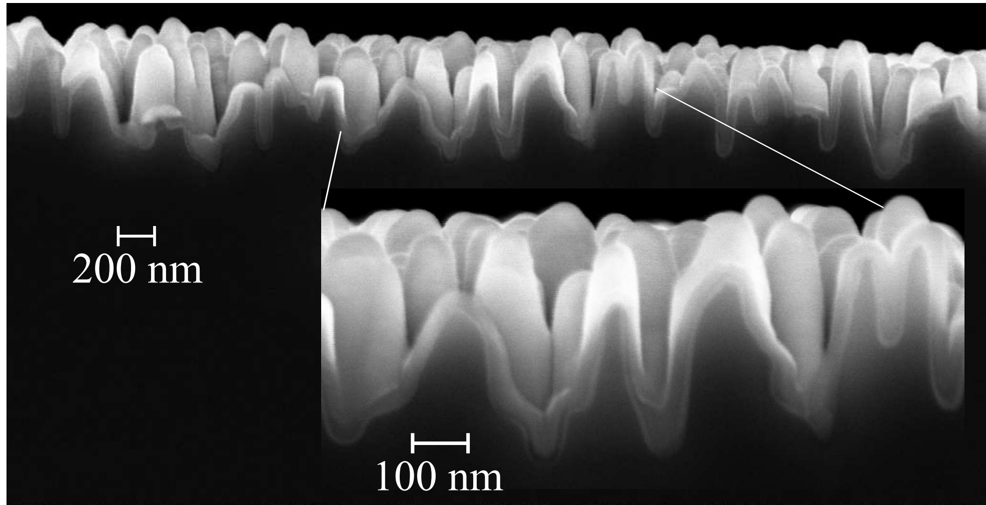

Figure 16: SEM image of b-Si covered with ALD SiO_2/Al_2O_3 dielectric stack. The films follow the nanostructured surface extremely well.

The nanostructures are approximately 500–700 nm high and several hundreds of nanometers wide based on the figure. Thus, the dimensions of the silicon needles are slightly smaller than reported in earlier studies [7], although the texture was etched with the same tool and identical process parameters. The difference is predominantly due to a different processing history of the tool in the recent past prior to the etching of the samples since the process is known to be highly sensitive on the prevailing conditions in the DRIE chamber [35]. Nevertheless, the sample looks black to a naked eye also with the dielectric film coverage, indicating that the reflectivity of the surface does not significantly differ from the reported optical properties. Thus, the surface morphology is relevant for the b-Si passivation studies.

4.4 Emitter formation

As the ALD SiO_2/Al_2O_3 stacks were found to contain positive fixed charge as predicted based on the literature (see Section 2.6.5), they were hypothesized to provide more efficient passivation for heavily doped n+ surfaces compared to bare Al_2O_3. Thus, those stacks were next applied to the actual research problem of interest, i.e. surface passivation of b-Si phosphorus emitters. First, the formation and properties of the emitters themselves are discussed.

P-type magnetic CZ silicon wafers with <100> orientation, 625 µm thickness and 20 Ωcm resistivity were used as starting material for the phosphorus emitter passivation study. The resistivity was chosen to be somewhat higher than in usual solar cell material since high injection condition necessary for reliable J_{0e} extraction, as described in Section 3.3, is challenging to achieve if the bulk material is heavily doped. Thus, the use of material with higher resistivity broadens the range of

J_{0e} values which can be reliably measured. Black silicon was first etched on both sides of HF-treated wafers with the same parameters as introduced in the previous section, followed by an SC1 cleaning and an HF-dip. Phosphorus diffusion was performed for the b-Si and planar reference wafers at either 800 °C or 830 °C (labelled POCL_800 and POCL_830, respectively) in a Centrotherm furnace. $POCl_3$ gas was introduced for 20 minutes, followed by a five-minute drive-in oxidation. Temperature was ramped up and down in nitrogen ambient.

Although the effect of a nanostructured surface on phosphorus diffusion is not completely understood and only a few studies regarding the topic have been published [39, 40], b-Si was etched prior to the diffusion since the opposite order, black silicon on emitter (BSOE), has its own limitations. In order to obtain high enough doping concentration in the emitter region with the BSOE process, extremely deep doping profile must be achieved since the etching removes approximately 2 μm of Si from the surface.

The applied diffusion process at 830 °C was known to result in a sheet resistance of 90–100 Ω/□ in planar wafers. However, applying standard diffusion conditions designed for planar surfaces also for b-Si results in excessive doping in the nanostructures and hence enhances Auger recombination, which eventually reduces the cell efficiency, as discussed in Section 2.5.1. Therefore, the diffusion process for the other sample set was performed at a lower temperature in order to reduce the surface doping concentration and to target a more reasonable sheet resistance value in b-Si.

Thickness of the grown phosphosilicate glass was measured with ellipsometer. Diffusion at 800 °C grew a 27–28 nm thick PSG, whereas 830 °C resulted in an oxide thickness of 33–34 nm. In addition, the conformality of the grown PSG layer on b-Si was inspected with SEM (Fig. 17). As can be seen from the figure, the glass was deposited rather conformally on the nanostructures, even at the bottom of the grooves. This was to be expected since PSG growth is essentially an oxidation process which consumes silicon from the wafer surface.

The PSG was removed in 5 vol-% HF-solution. Profiles of electrically active phosphorus concentration in the emitter region were measured from the planar samples with electrochemical capacitance–voltage profiling method and are shown in Fig. 17. In addition, a total P concentration profile was measured from a sample doped at 830 °C with SIMS. The ECV tool was observed to systematically etch more than it reported, verified by profilometer measurements. Therefore, the ECV data has been corrected assuming the etch rate and hence the error per unit length to be independent of depth. Profiles in b-Si were not measured due to instrumental limitations to measure doping concentration in the case of nanostructured surfaces accurately. Sheet resistance was measured from both planar and b-Si samples with four-point probe and confirmed later by an inductive coupling based method with Sinton lifetime tester.

The difference between the total and electrically active phosphorus concentration in the POCL_830 profiles near the sample surface indicates the presence of inactive dopants. Moreover, based on the sheet resistance values shown as an inset in Fig. 17, the enhanced surface area of b-Si resulted in a larger amount of P in those emitters,

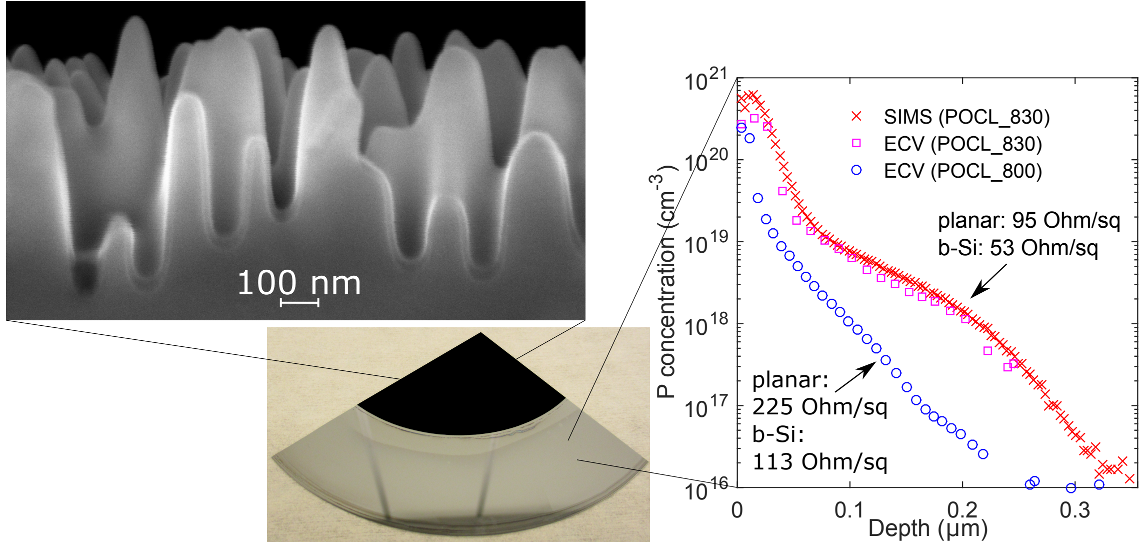

Figure 17: Left: SEM image of PSG on top of a b-Si structure indicating conformal surface coverage. Right: Doping profiles of two planar samples measured with ECV. In addition, SIMS profile of POCL_830 diffused sample is presented. The measured sheet resistance values are shown as an inset, including b-Si samples. In the middle, a quarter of a 6" wafer with b-Si etched in the middle is shown. The reflectance of the nanostructured surface is near zero, as visible in the figure.

which is in accordance with the literature [6]. As the Si needles were covered with phosphosilicate glass from all sides, more phosphorus diffused into the substrate during the drive-in. Thus, a considerably higher amount of P in the b-Si samples was expected.

4.5 Phosphorus emitter passivation

After the preparation and characterization of the bare emitters, their surface passivation with ALD thin films was studied. A planar and a b-Si sample were processed simultaneously in all process steps. After PSG removal, the samples were passivated with either a stack of 6.5 nm of plasma-enhanced ALD SiO_2 and 30 nm of Al_2O_3 or only 22 nm of ALD Al_2O_3 for a comparison. Based on the process development for the deposition of SiO_2/Al_2O_3 stacks presented in Section 4.3, the deposition scheme labelled with #2, i.e. a double pulse process on an HF-dipped surface, was chosen for these experiments. For the bare Al_2O_3 deposition, no specific process development was performed, since the optimization was already conducted for a previous study [7]. Directly after the deposition, J_{0e} was extracted from the measured QSSPC data at a high injection level (10^{16}cm^{-3} for most of the samples) based on the method described in Section 3.3. However, neither of the films passivated the surfaces sufficiently in the as-deposited state. The samples were subsequently annealed at 400 °C in nitrogen and J_{0e} provided by the annealed film measured in a similar way. One planar lifetime reference sample was processed in all ALD runs with the emitter samples in order to confirm that the process functioned properly

and to allow the determination of Q_{tot} and D_{it} of the deposited films.

Fig. 18a presents emitter saturation current densities for both planar and b-Si samples with two different emitter profiles, POCL_830 and POCL_800, and two different ALD passivation schemes. As hypothesised, the SiO_2/Al_2O_3 stacks provide lower J_{0e} values compared to bare Al_2O_3 in all cases. This can mainly be attributed to the more suitable polarity of the oxide charge as shown in Fig. 18b. Although the absolute value of Q_{tot} is lower in the oxide stack, it outperforms the negatively charged Al_2O_3 in J_{0e}. Better passivation provided by the SiO_2/Al_2O_3 stacks can partly be explained also by the lower mid-gap interface defect density as presented in Fig. 18b. The D_{it} is again reported only for the planar samples. The improvement is more significant in the samples with lower doping (i.e. POCL_800), which can be attributed to a smaller amount of inactive P and less dominating Auger recombination.

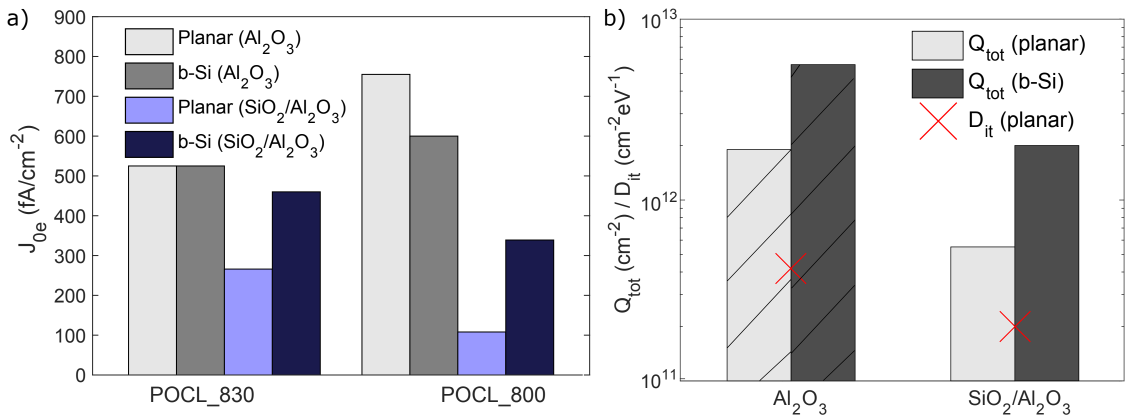

Figure 18: a) Emitter saturation current density of phosphorus emitter samples passivated with either bare Al_2O_3 or SiO_2/Al_2O_3 stacks. b) Total charge and interface defect density of the dielectric layers after annealing. The charge of bare Al_2O_3 was negative as indicated by the diagonal stripes. D_{it} values have been determined from the planar samples.

The J_{0e} values obtained from the planar samples with the stacks are in accordance with results reported by Bordihn *et. al.* [77]. The POCL_830 profile shown in Fig. 17 corresponds the reported profile with 72 Ω/□ sheet resistance rather well. The authors achieved a J_{0e} of approximately 200 fA/cm^2 with their SiO_2/Al_2O_3 stack with PECVD SiO_2 interlayer which is only slightly lower than the value obtained in this study.

Approximately three times higher effective charge density was measured from b-Si samples compared to the planar references, which is in agreement with the previously reported results [8], the relative difference being slightly higher in the case of the stacks. However, the lowest J_{0e} values were obtained with planar surfaces, b-Si enhancing both Auger and surface recombination by altering the doping profile and increasing the surface area, respectively [6].

The surface passivation quality, as characterized by D_{it} and Q_{tot}, indicated better J_{0e} values than were measured in samples passivated with the stacks. In order

to study whether the reason for rather high J_{0e} values was due to insufficient level of field-effect passivation or emitter recombination, positive corona charge was deposited onto the samples. Various amounts of corona were deposited onto both sides of the samples with Semilab LCC-300 Linear Corona Charger. The actual amount of deposited charge was determined by measuring the contact potential difference between a Kelvin probe and the silicon substrate before and after every deposition step using method described in Section 3.5. Dielectric constants of 3.9 and 7 for SiO_2 and Al_2O_3, respectively, and actual film thicknesses measured with ellipsometer were used in Eq. 42 . A single corona charge deposition step deposits a smaller areal charge density on b-Si compared to a planar surface since equal amount of ions is distributed onto a larger area (recall Fig. 6). Nevertheless, the contact potential difference method takes this phenomenon into account.

In Fig. 19, J_{0e} as a function of deposited corona charge density is presented for the same samples. J_{0e} of the Al_2O_3 passivated samples (both planar and b-Si) was reduced substantially by the deposition of positive charge, which is natural and in agreement with previously reported results [76]. On the contrary, positive corona charge had barely any impact on the stacks. Furthermore, J_{0e} saturated to approximately same value for both Al_2O_3 and SiO_2/Al_2O_3 passivated samples. Thus, this value can be considered as the J_{0e} limited by Auger recombination and a dead layer caused by inactive P. The saturation of J_{0e} can also partly be due to additional interface defects introduced by the corona charging [90], although evidence for also non-invasive nature of corona with rather weak electric fields exists [93]. The Auger limit is considerably higher for the b-Si samples due to the higher doping concentration. Therefore, lower values could be achieved only by designing the emitter profiles further in order to avoid excessive doping and dead layer formation. Similar trends are observed with both diffusion profiles, the effect of corona charge being more significant in the case of POCL_800 profile. The larger improvement in the samples with less doping is due to less dominating Auger recombination, in which case the surface passivation has more importance.

The lower limits of J_{0e} are significantly higher than 50 fA/cm^2 reported by van de Loo *et. al.* [76]. Nevertheless, van de Loo's emitter had substantially lighter dose. The reported electrically active surface doping concentration in the 110 $\Omega/\Box$ n+ emitter was equally high, but otherwise the doping concentration was lower. This reduced the Auger limit and hence enabled lower J_{0e} values compared to this study. Moreover, the large amount of inactive phosphorus in the processed samples increased recombination losses in the emitter further, which is not visible in the ECV profiles.

In the case of b-Si samples, slightly lower J_{0e} values were obtained with bare Al_2O_3 than with the stacks by corona charging. This could be explained by weaker chemical passivation provided by the stacks in the case of b-Si, opposite to what observed from planar samples by COCOS method. However, the interface quality on b-Si cannot be directly concluded from the D_{it} values measured from corresponding planar samples. For instance, rather short ALD pulses and purges may provide excellent thin film quality on planar surfaces, but result in a non-conformal film on b-Si.

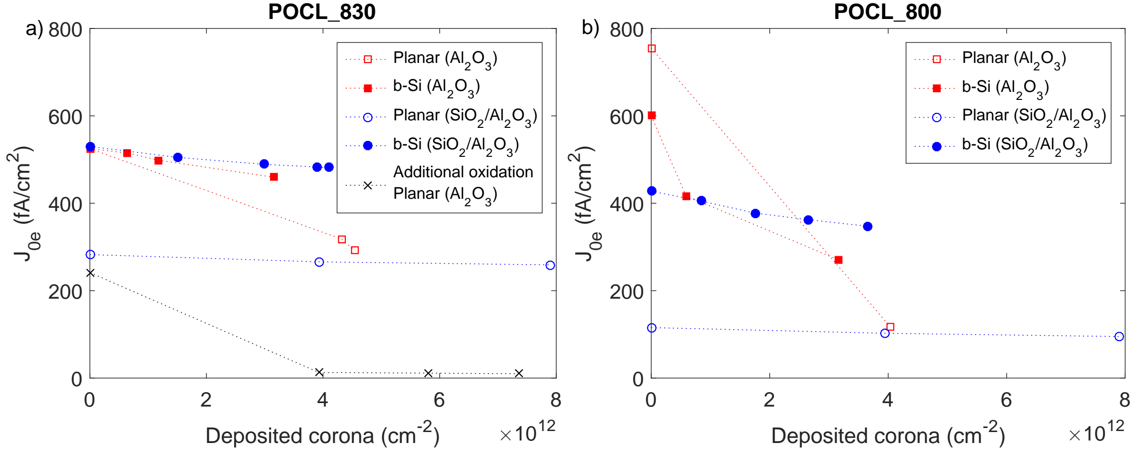

Figure 19: J_{0e} as a function of deposited corona charge density for two different emitter profiles: a) POCL_830 and b) POCL_800. Open symbols denote planar and filled symbols b-Si samples. The deposited charge reduces the J_{0e} of the Al_2O_3 passivated samples considerably, while it has barely any impact on the SiO_2/Al_2O_3 passivated samples. In the samples with lighter doping (i.e. POCL_800), the effect is more significant. The Auger limited J_{0e} is higher in the b-Si samples. In addition, J_{0e} of a planar sample with lower surface doping concentration achieved with additional oxidation is presented (black crosses).

In order to reduce the surface concentration and the amount of inactive phosphorus, one planar wafer originally doped with the POCL_830 profile was oxidized at 800 °C for 1 h. The PSG was removed prior to the oxidation in order to remove the phosphorus source. Otherwise the surface doping concentration would have remained rather constant and the amount of doping increased instead, since the PSG layer would have acted as an unlimited phosphorus source at the wafer surface. The oxidation parameters were replicated from [94] and [95], where the P surface concentration was shown to be reduced below the upper limit of electrically active phosphorus concentration and the dead layer to be removed from the surface. The original doping profile (i.e., POCL_830) was approximately identical to the reported starting profiles.

Based on the references for the oxidation parameters ([94] and [95]), the high-temperature step in O_2 ambient changes the doping profile but keeps the sheet resistance rather constant since the amount of phosphorus in the wafer is unchanged. However, a sheet resistance of 220 Ω/□ was measured from the wafer after the oxidation. Reason for this unexpected behaviour is assumed to be in the cleaning sequences performed to the doped sample. The wafer underwent the standard cleaning procedure prior to the oxidation which etched heavily phosphorus doped silicon from the wafer surface and hence reduced the doping concentration significantly.

J_{0e} of 59 fA/cm^2 was measured from the sample passivated with thermal oxide grown during the above-mentioned oxidation step. Subsequently, the oxide was removed in HF and the same sample was passivated with ALD Al_2O_3. This passivation scheme yielded a J_{0e} of 242 fA/cm^2 which is naturally higher than that obtained

with thermal oxide due to the unsuitable polarity of fixed charge. Nevertheless, the J_{0e} was reduced to as low as 9.9 fA/cm^2 by deposition of positive corona charge as shown with black crosses in Fig. 19. This final value is lower than that achieved with thermal oxide which can mainly be attributed to a higher amount of positive charge at the surface due to the corona deposition.

5 Conclusions

Black silicon has been of interest of the photovoltaic community already some time due to its excellent light absorption properties. The difficulties in the surface passivation of b-Si have recently been overcome with ALD Al_2O_3 [7] and impressive results have been published with n-type solar cells consisting of p+ emitter [25]. However, there is no solution yet presented for the dominating p-type solar cells with an n+ emitter as Al_2O_3 provides only limited passivation for such emitters due to its negative fixed charge. This problem is enhanced in b-Si, which relies more heavily on the field-effect passivation [8]. Thus, in order to make b-Si a viable option for current photovoltaic industry, a passivation material with positive fixed charge is required.

The goal of this thesis was to solve the above-mentioned problem by finding a material with positive fixed charge and low interface defect density and demonstrate its passivation efficiency on black silicon n+ emitter doped with phosphorus. According to literature, a SiO_2 interlayer between an Al_2O_3 thin film and a silicon substrate prevents the negative charge formation in the uppermost layer and a positive fixed charge density can be obtained instead. Thus, SiO_2/Al_2O_3 dielectric stacks were selected and studied experimentally on phosphorus doped b-Si surfaces.

First, electrical properties of stacks with either thermal or PEALD SiO_2 interlayer were compared using minority carrier lifetime and contactless C–V measurements. As expected based on the literature, the interlayer deposited with ALD was found to be able to prevent the detrimental negative charge formation in the Al_2O_3 layer, contrary to thermal SiO_2. Furthermore, both stacks provided low interface defect density in the order of 10^{11} $cm^{-2}eV^{-1}$ on silicon. In addition, SEM images revealed that the ALD thin films coated b-Si surfaces conformally, which is essential for efficient passivation of the nanostructures. Contrary to the hypothesis on enhanced passivation, diluted SC2 pretreatment resulted in negative polarity of fixed charge in the thin film stack. Although the interface defect density was further reduced, this pretreatment was discarded as a viable option due to the unfavourable charge polarity.

The ALD SiO_2/Al_2O_3 stacks were then applied to b-Si phosphorus emitters. The positive fixed charge in the stacks resulted in lower emitter saturation current densities compared to bare Al_2O_3 as expected. The stacks were found to passivate planar emitters efficiently and the measured J_{0e} values were comparable to those reported in literature [77]. They worked surprisingly well also on b-Si which has not been reported earlier. The level achieved on planar surfaces could not be reached on b-Si but it was expected due to a larger surface area and enhanced phosphorus diffusion. Since the optimization of the emitter itself was not within the scope of this thesis, the b-Si emitter suffered from enhanced excessive doping and a large amount of inactive phosphorus. This resulted in significant Auger recombination, which was verified by corona charging experiments, and limited the measured emitter saturation current density. Nevertheless, the results suggest that the actual surface passivation works which was the goal of this study. The results thus provide a significant step towards the implementation of b-Si for commercial p-type silicon

solar cells.

The next logical step is to study surface passivation provided by the SiO_2/Al_2O_3 stacks on emitters with a more advanced phosphorus profile in order to demonstrate the true potential of the stacks. More freedom to the control of dopant concentration can be achieved with ion implantation which will be used to prepare the next samples. The results achieved in this work have interested a leading solar cell manufacturer as they show for the first time that the implementation of b-Si for commercial p-type silicon solar cells is feasible. The company has offered a possibility to apply the stacks to their industrial emitters and demonstrate their capability in prototype b-Si solar cells which will be manufactured in the pilot production line of the company. Thus, the results will directly be piloted at the industrial scale.

As b-Si obviates the need of AR coatings and traditional surface texturization, its implementation will reduce both material and production costs of solar cells. Thus, by making b-Si a viable option for PV industry, this thesis enables an enhancement in the cost efficiency of solar cells and hence makes the utilization of solar energy more economical. Ultimately, this brings solar power one step closer to its final breakthrough and the humankind towards a CO_2 emission free world.

References

[1] Perez, R. and Perez, M. A fundamental look at energy reserves for the planet. *The IEA SHC Solar Update*, vol. 50, pp. 2–3, 2009.

[2] Green, M. A. *Solar cells: operating principles, technology, and system applications.* Prentice-Hall, Englewood Cliffs, New Jersey, 1982. ISBN 0-13-82270.

[3] Palik, E. D. *Handbook of Optical Constants of Solids.* Academic Press, Boston, 1985. ISBN 978-0-12-544415-6.

[4] Clapham, P. B. and Hutley, M. C. Reduction of lens reflection by the "Moth Eye" principle. *Nature*, vol. 244, pp. 281–282, 1973. doi:10.1038/244281a0.

[5] Stepehns, R. B. and Cody, G. D. Optical reflectance and transmission of a textured surface. *Thin Solid Films*, vol. 45, pp. 19–29, 1977. doi:10.1016/0040-6090(77)90197-3.

[6] Oh, J., Yuan, H. and Branz, H. M. An 18.2%-efficient black-silicon solar cell achieved through control of carrier recombination in nanostructures. *Nature Nanotechnology*, vol. 7, pp. 743–748, 2012. doi:10.1038/NNANO.2012.166.

[7] Repo, P., Haarahiltunen, A., Sainiemi, L., Yli-Koski, M., Talvitie, H., Schubert, M. C. and Savin, H. Effective passivation of black silicon surfaces by atomic layer deposition. *IEEE Journal of Photovoltaics*, vol. 3, no. 1, pp. 90–94, 2013. doi:10.1109/jphotov.2012.2210031.

[8] von Gastrow, G., Alcubilla, R., Ortega, P., Yli-Koski, M., Conesa-Boj, S., Fontcuberta i Morral, A. and Savin, H. Analysis of the atomic layer deposited Al_2O_3 field-effect passivation in black silicon. *Solar Energy Materials and Solar Cells*, vol. 142, no. 11, pp. 29–33, 2015. doi:10.1016/j.solmat.2015.05.027.

[9] Repo, P., Benic, J., von Gastrow, G., Vähänissi, V., Friedemann, D. H., Schön, J., Schubert, M. C. and Savin, H. Passivation of black silicon boron emitters with atomic layer deposited aluminum oxide. *physica status solidi (RRL) - Rapid Research Letters*, vol. 7, no. 11, pp. 950–954, 2013. doi:10.1002/pssr.201308096.

[10] Colville, F. Why p-type multi c-Si is seeing strong market-share gains. *Photovoltaics International*, vol. 26, 2015.

[11] Hoex, B., van de Sanden, M. C. M., Schmidt, J., Brendel, R. and Kessels, W. M. M. Surface passivation of phosphorus-diffused n^+-type emitters by plasma-assisted atomic-layer deposited Al_2O_3. *physica status solidi (RRL) - Rapid Research Letters*, vol. 6, no. 1, pp. 4–6, 2012. doi:10.1002/pssr.201105445.

[12] Franssila, S. *Introduction to Microfabrication.* Wiley, Chichester, 2004. ISBN 9786610275014.

[13] Hall, R. N. Electron–hole recombiantion in germanium. *Physical Review*, vol. 87, no. 2, p. 387, 1952. doi:10.1103/PhysRev.87.387.

[14] Shockley, W. and Read, W. T. Statistics of the recombinations of holes and electrons. *Physical Review*, vol. 87, no. 5, p. 835, 1952. doi:10.1103/PhysRev.87.835.

[15] Schroder, D. K. *Semiconductor material and device characterization.* 3 ed. John Wiley & Sons, Inc., Hoboken, New Jersey, 2006. ISBN 0-471-73906-5.

[16] Varshni, Y. P. Band-to-band radiative recombination in groups IV, VI and III-V semiconductors. *physica status solidi (b) - Basic Solid State Physics*, vol. 19, no. 2, pp. 459–514, 1967. doi:10.1002/pssb.19670190202.

[17] Hall, R. N. Recombination processes in semiconductors. *Proceedings of the IEE - Part B: Electronic and Communication Engineering*, vol. 106, no. 17, pp. 923–931, 1959. doi:10.1049/pi-b-2.1959.0171.

[18] Balkanski, M. and Wallis, R. F. *Semiconductor physics and applications.* Oxford University Press, 2000. ISBN 978-1-61344-549-5.

[19] Sproul, A. B. Dimensioless solution of the equation describing the effect of surface recombination on carrier decay in semiconductors. *Journal of Applied Physics*, vol. 76, no. 5, pp. 2851–2854, 1994. doi:10.1063/1.357521.

[20] Aberle, A. G. Surface passivation of crystalline silicon solar cells: A review. *Progress in Photovoltaics: Research and Applications*, vol. 8, no. 5, pp. 473–487, 2000. doi:10.1002/1099-159X(200009/10)8:5<473::AID-PIP337>3.0.CO;2-D.

[21] Hu, C. C. *Modern Semiconductor Devices for Integrated Circuits.* Pearson Higher Education, 2010. ISBN 978-0-13-608525-6.

[22] Hoex, B., Schmidt, J., Bock, R., Altermatt, P. P., van de Sanden, M. C. M. and Kessels, W. M. M. Excellent passivation of highly doped p-type Si surfaces by the negative-charge-dielectric Al_2O_3. *Applied Physics Letters*, vol. 91, no. 11, p. 112107, 2007. doi:10.1063/1.2784168.

[23] Green, M. A. Self-consistent optical parameters of intrinsic silicon at 300 K including temperature coefficients. *Solar Energy Materials and Solar Cells*, vol. 92, no. 11, pp. 1305–1310, 2008. doi:10.1016/j.solmat.2008.06.009.

[24] Basu, P. K., Sarangi, D., Shetty, K. D. and Boreland, M. B. Light trapping in silicon nanowire solar cells. *Solar Energy Materials and Solar Cells*, vol. 113, pp. 37–43, 2013. doi:10.1016/j.solmat.2013.01.037.

[25] Savin, H., Repo, P., von Gastrow, G., Ortega, P., Calle, E., Garin, M. and Alcubilla, R. Black silicon solar cells with interdigitated back-contacts achieve 22.1% efficiency. *Nature Nanotechnology*, vol. 10, pp. 624–628, 2015. doi:10.1038/nnano.2015.89.

[26] Sihvola, A. and Lindell, I. *Sähkömagneettinen kenttäteoria 2: Dynaamiset kentät*. 5 ed. Otatieto, 2004. ISBN 9789516723405.

[27] Repo, P., Benic, J., Vähänissi, V., Schön, J., von Gastrow, G., Steinhauser, B., Schubert, M. C., Hermle, M. and Savin, H. N-type black silicon solar cells. *Energy Procedia*, vol. 38, pp. 866–871, 2013. doi:10.1016/j.egypro.2013.07.35.

[28] Bett, A. J., Eisenlohr, J., Höhn, O., Repo, P., Savin, H., Bläsi, B. and Goldschmidt, C. Wave optical simulation of the light trapping properties of black silicon surface textures. *Optics Express*, vol. 24, no. 6, pp. A434–A445, 2016. doi:10.1364/OE.24.00A434.

[29] Huang, Z., Geyer, N., Werner, P., de Boor, J. and Gösele, U. Metal-assisted chemical etching of silicon: A review. *Advanced Materials*, vol. 23, no. 2, pp. 285–308, 2010. doi:10.1002/adma.201001784.

[30] Her, T.-H., Finlay, R. J., Wu, C., Deliwala, S. and Mazur, E. Microstructuring of silicon with femtosecond laser pulses. *Applied Physics Letters*, vol. 73, no. 12, pp. 1673–1675, 1998. doi:10.1063/1.122241.

[31] Garnett, E. and Yang, P. Light trapping in silicon nanowire solar cells. *Nano Letters*, vol. 10, no. 3, pp. 1082–1087, 2010. doi:10.1021/nl100161z.

[32] Jansen, H., de Boer, M., Legtenberg, R. and Elwenspoek, M. The black silicon method: a universal method for determining the parameter setting for a fluorine-based reactive ion etcher in deep silicon trench etching with profile control. *Journal of Micromechanics and Microengineering*, vol. 5, no. 2, pp. 115–120, 1995. doi:10.1088/0960-1317/5/2/015.

[33] Mellhaoui, X., Dussart, R., Tillocher, T., Lefaucheux, P., Ranson, P., Boufnichel, M. and Overzet, L. J. SiO_xF_y passivation layer in silicon cryoetching. *Journal of Applied Physics*, vol. 98, no. 10, p. 104901, 2005. doi:10.1063/1.2133896.

[34] Legtenberg, R., Jansen, H., de Boer, M. and Elwenspoek, M. Anisotropic reactive ion etching of silicon using $SF_6/O_2/CHF_3$ gas mixtures. *Journal of The Electrochemical Society*, vol. 142, no. 6, pp. 2020–2028, 1995. doi:10.1149/1.2044234.

[35] Sainiemi, L., Jokinen, V., Shah, A., Shpak, M., Aura, S., Suvanto, P. and Franssila, S. Non-reflecting silicon and polymer surface by plasma etching and replication. *Advanced Materials*, vol. 23, no. 1, pp. 122–126, 2010. doi:10.1002/adma.201001810.

[36] Hoex, B., Gielis, J. J. H., van de Sanden, M. C. M. and Kessels, W. M. M. On the c-Si surface passivation mechanism by the negative-charge-dielectric Al_2O_3. *Journal of Applied Physics*, vol. 104, no. 11, p. 113703, 2008. doi:10.1063/1.3021091.

[37] Yuan, H.-C., Yost, V. E., Page, M. R., Stradins, P., Meier, D. L. and Branz, H. M. Efficient black silicon solar cell with a density-graded nanoporous surface: Optical properties, performance limitations, and design rules. *Applied Physics Letters*, vol. 95, no. 12, p. 123501, 2009. doi:10.1063/1.3231438.

[38] Liu, W. F., Bian, J. M., Zhao, Z. C., Luo, Y. L., Yuan, Z., Zhang, B. Y. and Liu, A. M. Low temperature surface passivation of black silicon solar cells by high-pressure O_2 thermal oxidation. *ECS Solid State Letters*, vol. 2, no. 4, pp. Q17–Q20, 2013. doi:10.1149/2.003304ssl.

[39] Kafle, B., Schön, J., Fleischmann, C., Werner, S., Wolf, A., Clochard, E., L. Duffy, Hofmann, M. and Rentsch, J. On the emitter formation in nanotextured silicon solar cells to achieve improved electrical performances. *Solar Energy Materials and Solar Cells*, vol. 152, pp. 94–102, 2016. doi:10.1016/j.solmat.2016.03.031.

[40] Shen, Z., Liu, B., Xia, Y., Liu, J., Liu, J., Zhong, S. and Li, C. Black silicon on emitter diminishes the lateral electric field and enhances the blue response of a solar cell by optimizing depletion region uniformity. *Scripta Materialia*, vol. 68, no. 3–4, pp. 199–202, 2013. doi:10.1016/j.scriptamat.2012.10.023.

[41] Hoex, B., Heil, S. B. S., Langereis, E., van de Sanden, M. C. M. and Kessels, W. M. M. Ultralow surface recombination of c-Si substrates passivated by plasma-assisted atomic layer deposited Al_2O_3. *Applied Physics Letters*, vol. 89, no. 4, p. 042112, 2006. doi:10.1063/1.2240736.

[42] Hoex, B., Schmidt, J., Pohl, P., van de Sanden, M. C. M. and Kessels, W. M. M. Silicon surface passivation by atomic layer deposited Al_2O_3. *Journal of Applied Physics*, vol. 104, no. 4, p. 044903, 2008. doi:10.1063/1.2963707.

[43] Weber, J. R., Janotti, A. and van de Walle, C. G. Native defects in Al_2O_3 and their impact on III-V/Al_2O_3 metal-oxide-semiconductor-based devices. *Journal of Applied Physics*, vol. 109, no. 3, p. 033715, 2011. doi:10.1063/1.3544310.

[44] Johnson, R. S., Lucovsky, G. and Baumvol, I. Physical and electrical properties of noncrystalline Al_2O_3 prepared by remote plasma enhanced chemical vapor deposition. *Journal of Vacuum Science and Technology A*, vol. 19, no. 4, pp. 1353–1360, 2001. doi:10.1116/1.1379316.

[45] Wang, W.-C., Lin, C.-W., Chen, H.-J., Chang, C.-W., Huang, J.-J., Yang, M.-J., Tjahjono, B., Huang, J.-J., Hsu, W.-C. and Chen, M.-J. Surface passivation of efficient nanotextured black silicon solar cells using thermal atomic layer deposition. *ACS Applied Materials and Interfaces*, vol. 5, no. 19, pp. 9752–9759, 2013. doi:10.1021/am402889k.

[46] Wang, W.-C., Tsai, M.-C., Yang, J., Hsu, C. and Chen, M.-J. Efficiency enhancement of nanotextured black silicon solar cells using Al_2O_3/TiO_2 dual-layer

passivation stack prepared by atomic layer deposition. *ACS Applied Materials and Interfaces*, vol. 7, no. 19, pp. 10228–10237, 2015. doi:10.1021/acsami.5b00677.

[47] Suh, D., Choi, D.-Y. and Weber, K. J. Al_2O_3/TiO_2 stack layers for effective surface passivation of crystalline silicon. *Journal of Applied Physics*, vol. 114, no. 15, p. 154107, 2013. doi:10.1063/1.4825258.

[48] Eades, W. D. and Swanson, R. M. Calculation of surface generation and recombination velocities at the $Si - SiO_2$ interface. *Journal of Applied Physics*, vol. 58, no. 11, pp. 4267–4276, 1985. doi:10.1063/1.335562.

[49] Stephens, A. W., Aberle, A. G. and Green, M. A. Surface recombination velocity measurements at the silicon–silicon dioxide interface by microwave-detected photoconductance decay. *Journal of Applied Physics*, vol. 76, no. 1, pp. 363–370, 1994. doi:10.1063/1.357082.

[50] Glunz, S. W., Sproul, A. B., Warta, W. and Wettling, W. Injection-level-dependent recombination velocities at the $Si - SiO_2$ interface for various dopand concentrations. *Journal of Applied Physics*, vol. 75, no. 3, pp. 1611–1615, 1994. doi:10.1063/1.356399.

[51] Cuevas, A., Basore, P. A., Giroult-Matlakowski, G. and Dubois, C. Surface recombination velocity of highly doped n-type silicon. *Journal of Applied Physics*, vol. 80, no. 6, pp. 3370–3375, 1996. doi:10.1063/1.363250.

[52] Kerr, M. J., Schmidt, J., Cuevas, A. and Bultman, J. H. Surface recombination velocity of phosphorus-diffused silicon solar cell emitters passivated with plasma enhanced chemical vapor deposited silicon nitride and thermal silicon oxide. *Journal of Applied Physics*, vol. 89, no. 7, pp. 3821–3826, 2001. doi:10.1063/1.1350633.

[53] Toor, F., Branz, H. M., Page, M. R., Jones, K. M. and Yuan, H.-C. Multi-scale surface texture to improve blue response of nanoporous black silicon solar cells. *Applied Physics Letters*, vol. 99, no. 10, p. 103501, 2011. doi:10.1063/1.3636105.

[54] Yoo, J. S., Parm, I. O., Gangopadhyay, U., Kim, K., Dhungel, S. K., Mangalaraj, D. and Yi, J. Black silicon layer formation for application in solar cells. *Solar Energy Materials and Solar Cells*, vol. 90, no. 18–19, pp. 3085–3093, 2006. doi:10.1016/j.solmat.2006.06.015.

[55] Vanheusden, K. and Stesmans, A. Positive charging of buried SiO_2 by hydrogenation. *Applied Physics Letters*, vol. 64, no. 19, pp. 2575–2577, 1994. doi:10.1063/1.111530.

[56] Afanas'ev, V. V. and Stesmans, A. Positive charging of thermal $SiO_2/(100)$ si interface by hydrogen annealing. *Applied Physics Letters*, vol. 72, no. 1, pp. 79–81, 1998. doi:10.1063/1.120650.

[57] Hezel, R. and Schörner, R. Plasma Si nitride - A promising dielectric to achieve high-quality silicon MIS/IL solar cells. *Journal of Applied Physics*, vol. 52, no. 4, pp. 3076–3079, 1981. doi:10.1063/1.3290583.

[58] Nagel, H., Aberle, A. G. and Hezel, R. Optimized antireflection coatings for planar silicon solar cells using remote PECVD silicon nitride and porous silicon dioxide. *Progress in Photovoltaics: Reseasrch and Applications*, vol. 7, no. 4, pp. 245–260, 1999. doi:10.1002/(SICI)1099-159X(199907/08)7:4<245::AID-PIP255>3.0.CO;2-3.

[59] Otto, M. *Effective Passivation of Black Silicon Surfaces by Conformal Thermal ALD Deposited Al_2O_3 Layers*. Ph.D. thesis, Faculty of Natural Sciences II - Chemistry, Physics and Mathematics. Martin-Luther-Universität Halle-Wittenberg, 2015.

[60] Liu, J., Liu, B., Shen, Z., Liu, J., Zhong, S., Liu, S., Li, C. and Xia, Y. Characterization of PIII textured industrial multicrystalline silicon solar cells. *Solar Energy*, vol. 86, no. 10, pp. 3004–3008, 2012. doi:10.1016/j.solener.2012.07.006.

[61] Inomata, Y., Fukui, K. and Shirasawa, K. Surface texturing of large area multicrystalline silicon solar cells using reactive ion etching method. *Solar Energy Materials and Solar Cells*, vol. 48, no. 1–4, pp. 237–242, 1997. doi:10.1016/S0927-0248(97)00106-2.

[62] Yoo, J., Yu, G. and Yi, J. Large-area multicrystalline silicon solar cell fabrication using reactive ion etching (RIE). *Solar Energy Materials & Solar Cells*, vol. 95, no. 1, pp. 2–6, 2011. doi:10.1016/j.solmat.2010.03.029.

[63] Dimitrov, D. Z. and Du, C.-H. Crystalline silicon solar cells with micro/nano texture. *Applied Surface Science*, vol. 266, pp. 1–4, 2013. doi:10.1016/j.apsusc.2012.10.081.

[64] Olibet, S., Vallat-Sauvain, E. and Ballif, C. Model for a-Si:H/c-Si interface recombination based on the amphoteric nature of silicon dangling bonds. *Physical Review B*, vol. 76, no. 3, p. 035326, 2007. doi:10.1103/PhysRevB.76.035326.

[65] Liu, X., Coxon, P. R., Peters, M., Hoex, B., Cole, J. M. and Fray, D. J. Black silicon: fabrication methods, properties and solar energy applications. *Energy & Environmental Science*, vol. 7, no. 10, pp. 3223–3263, 2014. doi:10.1039/C4EE01152J.

[66] Montesdeoca-Santana, A., Ziegler, J., Lindekugel, S., Jiménez-Rodríguez, E., Keipert-Colberg, S., Müller, S., Krause, C., Borchert, D. and Guerrero-Lemus, R. A comparative study on different textured surfaces passivated with amorphous silicon. *physica status solidi (c)*, vol. 8, no. 3, pp. 747–750, 2011. doi:10.1002/pssc.201000234.

[67] Dingemans, G., Terlinden, N. M., Verheijen, M. A., van de Sanden, M. C. M. and Kessels, W. M. M. Controlling the fixed charge and passivation properties of Si(100)/Al_2O_3 interfaces using ultrathin SiO_2 interlayers synthesized by atomic layer deposition. *Journal of Applied Physics*, vol. 110, no. 9, p. 093715, 2011. doi:10.1063/1.3658246.

[68] Terlinden, N. M., Dingemans, G., Vandalon, V., Bosch, R. H. E. C. and Kessels, W. M. M. Influence of the SiO_2 interlayer thickness on the density and polarity of charges in Si/SiO_2/Al_2O_3 stacks as studied by optical second-harmonic generation. *Journal of Applied Physics*, vol. 115, no. 3, p. 033708, 2014. doi:10.1063/1.4857075.

[69] Razavy, M. *Quantum Theory of Tunneling*. World Scientific, 2003. ISBN 9789812564887.

[70] Mack, S., Wolf, A., Brosinsky, C., Schmeisser, S., Kimmerle, A., Saint-Cast, P., Hofmann, M. and Biro, D. Silicon surface passivation by thin thermal oxide/pecvd layer stack systems. *IEEE Journal of Photovoltaics*, vol. 1, no. 2, pp. 135–145, 2011. doi:10.1109/JPHOTOV.2011.2173299.

[71] Dingemans, G., Beyer, W., van de Sanden, M. C. M. and Kessels, W. M. M. Hydrogen induced passivation of Si interfaces by Al_2O_3 films and SiO_2/Al_2O_3 stacks. *Applied Physics Letters*, vol. 97, no. 15, p. 152106, 2010. doi:10.1063/1.3497014.

[72] Dingemans, G., van de Sanden, M. C. M. and Kessels, W. M. M. Excellent Si surface passivation by low temperature SiO_2 using an ultrathin Al_2O_3 capping film. *physica status solidi (RRL) - Rapid Research Letters*, vol. 5, no. 1, pp. 22–24, 2011. doi:10.1002/pssr.201004378.

[73] Dingemans, G., Einsele, F., Beyer, W., van de Sanden, M. C. M. and Kessels, W. M. M. Influence of annealing and Al_2O_3 properties on the hydrogen-induced passivation of the Si/SiO_2 interface. *Journal of Applied Physics*, vol. 111, no. 9, p. 093713, 2012. doi:10.1063/1.4709729.

[74] Bao, Y., Li, S., von Gastrow, G., Repo, P., Savin, H. and Putkonen, M. Effect of substrate pretreatments on the atomic layer deposited Al_2O_3 passivation quality. *Journal of Vacuum Science and Technology A*, vol. 33, no. 1, p. 01A123, 2015. doi:10.1116/1.4901456.

[75] Bordihn, S., Mertens, V., Engelhart, P., Kersten, F., Mandoc, M. M., Müller, J. W. and Kessels, W. M. M. Surface passivation by Al_2O_3 and $a-SiN_x$ films deposited on wet-chemically conditioned si surfaces. *ECS Journal of Solid State Science and Technology*, vol. 1, no. 6, pp. 320–325, 2012. doi:10.1149/2.008301jss.

[76] van de Loo, B. W. H., Knoops, H. C. M., Dingemans, G., Janssen, G. J. M., Lamers, M. W. P. E., Romijn, I. G., Weeber, A. W. and Kessels, W. M. M.

"Zero-charge" SiO_2/Al_2O_3 stacks for the simultaneous passivation of n^+ and p^+ doped silicon surfaces by atomic layer deposition. *Solar Energy Materials and Solar Cells*, vol. 143, pp. 450–456, 2015. doi:10.1016/j.solmat.2015.07.040.

[77] Bordihn, S., Dingemans, G., Mertens, V., Müller, J. W. and Kessels, W. M. M. Passivation of n^+ -type Si surfaces by low temperature processed SiO_2/Al_2O_3 Stacks. *IEEE Journal of Photovoltaics*, vol. 3, no. 3, pp. 925–929, 2013. doi: 10.1109/JPHOTOV.2013.2248415.

[78] Stevenson, D. T. and Keyes, R. J. Measurement of carrier lifetimes in germanium and silicon. *Journal of Applied Physics*, vol. 26, no. 2, pp. 190–195, 1955. doi:10.1063/1.1721958.

[79] Sinton, R. A., A., C. and Stuckings, M. Quasi-steady-state photoconductance, a new method for solar cell material and device characterization. *Photovoltaic Specialists Conference, 1996, Conference Record of the Twenty Fifth IEEE*, pp. 457–460. 1996. doi:10.1109/PVSC.1996.564042.

[80] Nagel, H., Berge, C. and Aberle, A. G. Generalized analysis of quasi-steady-state and quasi-transient measurements of carrier lifetimes in semiconductors. *Journal of Applied Physics*, vol. 86, no. 11, pp. 6218–6221, 1999. doi:10.1063/1.371633.

[81] Kane, D. E. and Swanson, R. M. Measurement of the emitter saturation current by a contactless photoconductivity decay method. *Proceedings of the 18th IEEE Photovoltaic Specialists Conference*, pp. 578–583. 1985.

[82] Richter, A., Glunz, S. W., Werner, F., Schmidt, J. and Cuevas, A. Improved quantitative description of auger recombination in crystalline silicon. *Physical Review B*, vol. 86, no. 16, p. 165202, 2012. doi:10.1103/PhysRevB.86.165202.

[83] Blum, A. L., Swirhun, J. S., Sinton, R. A. and Kimmerle, A. An updated analysis to the WCT-120 QSSPC measurement system using advanced device physics. *Proceedings of the 28th European Photovoltaic Solar Energy Conference and Exhibition*, pp. 1521–1523. 2013. doi:10.4229/28thEUPVSEC2013-2CV.3.3.

[84] Kimmerle, A., Rothhardt, P., Wolf, A. and Sinton, R. A. Increased reliability for J_{0e}-analysis by QSSPC. *Energy Procedia*, vol. 55, pp. 101–106, 2014. doi: 10.1016/j.egypro.2014.08.087.

[85] Kimmerle, A., Wolf, A., Belledin, U. and Biro, D. Modelling carrier recombination in highly phosphorus-doped industrial emitters. *Energy Procedia*, vol. 8, pp. 275–281, 2011. doi:10.1016/j.egypro.2011.06.136.

[86] Schenk, A. Finite-temperature full random-phase approximation model of band gap narrowing for silicon device simulation. *Journal of Applied Physics*, vol. 84, no. 7, pp. 3684–3695, 1998. doi:10.1063/1.368545.

[87] Wilson, M., Lagowski, J., Jastrzebski, L., Savtchouk, A. and Faifer, V. COCOS (corona oxide characterization of semiconductor) non-contact metrology for gate dielectrics. *AIP Conference Proceedings*, vol. 550, pp. 220–225, 2001. doi:10.1063/1.1354401.

[88] Shahin, M. M. Mass-spectrometric studies of corona discharges in air at atmospheric pressures. *The Journal of Chemical Physics*, vol. 45, no. 7, pp. 2600–2605, 1966. doi:10.1063/1.1727980.

[89] Shahin, M. M. Nature of charge carriers in negative coronas. *The Journal of Chemical Physics*, vol. 8, no. 101, pp. 106–110, 1969. doi:10.1364/AO.8.S1.000106.

[90] Stesmans, A. and Afanas'ev, V. V. Invasive nature of corona charging on thermal Si/SiO_2 structures with nanometer-thick oxides revealed by electron spin resonance. *Applied Physics Letters*, vol. 82, no. 17, pp. 2835–2837, 2003. doi:10.1063/1.1540245.

[91] Lagowski, J., Edelman, P. and Wilson, M. Measurement of the interface trap charge in an oxide semiconductor layer interface, 2000. US Patent 6,037,797.

[92] Kerr, M. J., Cuevas, A. and Sinton, R. A. Generalized analysis of quasi-steady-state and transient decay open circuit voltage measurements. *Journal of Applied Physics*, vol. 91, no. 1, pp. 399–404, 2002. doi:10.1063/1.1416134.

[93] Dautrich, M., Lenahan, P. M., Kang, A. Y. and Conley, J. F. Non-invasive nature of corona charging on thermal Si/SiO_2 structures. *Applied Physics Letters*, vol. 85, no. 10, pp. 1844–1845, 2004. doi:10.1063/1.1789576.

[94] Prajapati, V., Horzel, J., Choulat, P., Janssens, T., Poortmans, J. and Mertens, R. Oxidation enhanced diffusion on p-type PERC solar cells. *27th European Photovoltaic Solar Energy Conference and Exhibition*, pp. 680–685. 2012. doi:10.4229/27thEUPVSEC2012-2BO.7.6.

[95] Khandelwal, R., Windgassen, H., van Molken, J., Pletzer, T. M. and Kurz, H. Comparison of large area high ohmic emitter silicon solar cells with standard screen-printed contacts. *39th IEEE Photovoltaic Specialists Conference*, pp. 2217–2220. 2013. doi:10.1109/PVSC.2013.6744916.